Ultrasmall and Highly Dispersed Pt Entities Deposited on Mesoporous N-doped Carbon Nanospheres by Pulsed CVD for Improved HER

Sven Küspert, Ian E. Campbell, Zhiqiang Zeng, S. Esmael Balaghi, Niklas Ortlieb, Ralf Thomann, Markus Knäbbeler-Buß, Christopher S. Allen, Suzanne E. Mohney, and Anna Fischer**

Vapor-based deposition techniques are emerging approaches for the design of carbon-supported metal powder electrocatalysts with tailored catalyst entities, sizes, and dispersions. Herein, a pulsed CVD (Pt-pCVD) approach is employed to deposit different Pt entities on mesoporous N-doped carbon (MPNC) nanospheres to design high-performance hydrogen evolution reaction (HER) electrocatalysts. The influence of consecutive precursor pulse number (50-250) and deposition temperature (225–300 °C) are investigated. The Pt-pCVD process results in highly dispersed ultrasmall Pt clusters (≈1 nm in size) and Pt single atoms, while under certain conditions few larger Pt nanoparticles are formed. The best MPNC-Pt-pCVD electrocatalyst prepared in this work (250 pulses, 250 °C) reveals a Pt HER mass activity of 22.2 ± 1.2 A $\text{mg}^{-1}{}_{\text{Pt}}$ at -50 mV versus the reversible hydrogen electrode (RHE), thereby outperforming a commercially available Pt/C electrocatalyst by 40% as a result of the increased Pt utilization. Remarkably, after optimization of the Pt electrode loading, an ultrahigh Pt mass activity of 56 ± 2 A $\text{mg}^{-1}{}_{\text{Pt}}$ at -50 mV versus RHE is found, which is among the highest Pt mass activities of Pt single atom and cluster-based electrocatalysts reported so far.

1. Introduction

Catalyst development in the field of polymer exchange membrane water electrolysis (PEMWE) is a central point for the large-scale production of hydrogen as an energy carrier in the transition to a sustainable energy system. For the hydrogen evolution reaction (HER) the scarce and cost-intensive catalyst material platinum is used on the cathode side in PEMWE. State-of-the-art HER electrocatalysts are still carbon-supported platinum nanoparticles.[1] Noteworthily, for small Pt nanoparticles of 2 nm in diameter, only surface atoms contribute to the catalysis leaving ≈ 50% of the Pt atoms as unutilized spectator atoms.[2,3] In addition, the dispersion of the active Pt species on the support material plays a further role in electrocatalysis, as highly dispersed Pt species show a significantly higher Pt mass

---

S. Küspert, Z. Zeng, N. Ortlieb, A. Fischer
Institute of Inorganic and Analytical Chemistry (IAAC)
University of Freiburg
Albertstraße 21, 79104 Freiburg, Germany
E-mail: anna.fischer@ac.uni-freiburg.de

S. Küspert, Z. Zeng, S. E. Balaghi, N. Ortlieb, R. Thomann, A. Fischer
Freiburg Materials Research Center (FMF)
University of Freiburg
Stefan-Meier-Straße 21, 79104 Freiburg, Germany

I. E. Campbell, S. E. Mohney
Department of Materials Science and Engineering
The Pennsylvania State University
University Park
Pennsylvania 16802, USA
E-mail: mohney@psu.edu

The ORCID identification number(s) for the author(s) of this article can be found under https://doi.org/10.1002/smll.202311260

DOI: 10.1002/smll.202311260

Z. Zeng, N. Ortlieb, A. Fischer
Cluster of Excellence livMatS
Cluster of Excellence livMatS, University of Freiburg
Freiburg Germany

S. E. Balaghi, R. Thomann, A. Fischer
Freiburg Center for Interactive Materials and Bioinspired Technologies (FIT)
University of Freiburg
Georges-Köhler-Allee 105, 79110 Freiburg, Germany

M. Knäbbeler-Buß
Fraunhofer Institute for Solar Energy Systems ISE
Heidenhofstraße 2, 79110 Freiburg, Germany

C. S. Allen
Electron Physical Science Imaging Center
Diamond Light Source Ltd
Didcot, Oxfordshire OX11 0DE, UK

C. S. Allen
Department of Materials
University of Oxford
Oxford OX1 3HP, UK

S. E. Mohney
Freiburg Institute for Advanced Studies
University of Freiburg
Albertstraße 19, 79104 Freiburg, Germany

activity compared to less dispersed and agglomerated Pt species.[4–6] It is therefore desirable, to increase this Pt utilization by size decrease and enhancement of dispersion (even to the limit of the single atom) to enable atom-efficient electrocatalysis and reduce the costs of PEMWE systems.[1,7,8]

Access to carbon-supported catalyst materials with high Pt dispersion (clusters and single sites) is favored on engineered carbon supports.[6,9,10] Ideally such carbon supports offer a tailored nano-morphology, high graphitization, and heteroatom doping, as these result in high surface areas, high electrical conductivities, as well as enhanced metal-support interactions or binding motifs (as for single sites), respectively.[1,11] Even if several approaches have been reported, the deposition of Pt on such engineered carbon supports requires further improvement to achieve a maximum ratio of electroactive surface area to electrocatalyst mass used.[6,7,9,10]

Various Pt deposition methods have been developed, which can be divided into dry (mainly by ball milling),[12–14] wet chemical,[15–17] and vapor-based syntheses.[18–20] While dry and wet-chemical methods are relatively simple to realize, very small particle sizes with appropriate Pt loading and preserved substrate and catalyst structure are often associated with tedious multistep syntheses.[14,16]

By contrast, vapor-based Pt depositions can be carried out in a single manufacturing step, and high Pt dispersions with a narrow particle size distribution and strong interaction of the metal with the support can be realized.[21,22] Although the cost issue of precursors and process steps of vapor-based techniques compared to conventional synthesis routes seems critical, an increased Pt utilization, performance, and stability of catalysts synthesized by vapor-based methods may fuel an economic integration of such synthesis methods. Among vapor-based approaches atomic layer deposition (ALD) and chemical vapor deposition (CVD) are widespread techniques.[18] Pt-ALD[19,23,24] commonly uses a metalorganic Pt precursor and a gaseous co-reactant like H_2,[25] O_2,[19,26,27] O_2 in dry air[28] or ozone[29] to deposit Pt films or particles. Pt-CVD is a straight forward technique since only a Pt precursor and an inert carrier gas are required.[30] The process depends mostly on temperature, pressure of the precursor and carrier gases, and the support material with its surface functionalities.[30,31]

To the best of our knowledge, the CVD of Pt on powder materials using a Pt precursor and only an inert carrier gas was the subject of only a few articles.[9,10,30,32] Kim et al. investigated the deposition of Pt on carbon nanotubes by CVD using trimethyl(methylcyclopentadienyl) platinum ($MeCpPtMe_3$) under inert N_2, N_2/O_2, and N_2/H_2 and could achieve a Pt loading of ≈3–5 wt% and a Pt nanoparticle size of 1–2 nm.[32] In a follow-up study aiming at a higher Pt loading of 40 wt% with a Pt particle size of 1–2 nm, the target could be achieved only on surface-oxidatively-pretreated multiwalled carbon nanotubes and carbon black under N_2 at 300 °C reactor temperature.[30] Although the authors referred to their process as ALD, Song et al. used the precursor $MeCpPtMe_3$ but did not report the use of a co-reactant in their study of Pt single-atom catalysts at 230 °C prepared on metal–organic framework-derived N-doped carbon,[10] unlike the majority of studies that employ O_2[19,26] as a co-reactant. Interestingly, Lubers et al. used mass spectrometry to investigate the byproducts of $MeCpPtMe_3$ reacting with powdered carbon supports (Vulcan XC72R) to better understand the mechanisms behind early ALD cycles.[33] They found that $MeCpPtMe_3$ reacted on the carbon to produce methane and ethane without introduction of a co-reactant, indicating the removal of ligands from $MeCpPtMe_3$. By using a functionalized carbon with additional oxygen groups, they found a smaller Pt particle size with a higher dispersion that they assigned to an improved interaction between the precursor and the carbon support.

In this work, we use $MeCpPtMe_3$ in a pulsed Pt CVD (Pt-pCVD) process with no co-reactant on monodisperse mesoporous N-doped carbon (MPNC) nanospheres (nanosphere size 271 ± 29 nm, pore size 23 ± 3 nm) as the support. The effects of pulse number (50-250 pulses) and temperature (225-300 °C) on the resulting Pt entity size, crystallinity, and dispersion are investigated by in-depth material characterization including among others X-ray diffraction (XRD), aberration-corrected high angle annular dark field scanning transmission electron microscopy (ac-HAADF-STEM), STEM coupled with energy dispersive X-ray spectroscopy (STEM-EDS) tomography, X-ray absorption spectroscopy (XAS) and electrochemical CO stripping. While increasing the number of pulses leads to the increase of Pt loading, the largest Pt loading is achieved at a deposition temperature of 250 °C. Regardless of the temperature and the number of pulses used here, Pt deposition mainly results in Pt clusters with sizes ≈1 nm and Pt single atoms as well as ultra-high Pt dispersion. Using the synthesis temperature of 225 °C, solely Pt clusters and single sites are present on the monodisperse MPNC support. At increased temperature and number of cycles, a few larger crystalline Pt nanoparticles and agglomerates were found. The MPNC-Pt-pCVD materials prepared at 225, 250, and 300 °C were then compared to a commercial Pt/C electrocatalyst for their HER performance. The most-active MPNC-Pt-pCVD deposited at 250 °C outperformed the reference Pt/C electrocatalyst by 40% with a high Pt mass activity of 22.2 ± 1.2 A $mg^{-1}{}_{Pt}$ at -50 mV vs. reversible hydrogen electrode (RHE). Furthermore, an ultra-high Pt mass activity of 56 ± 2 A $mg^{-1}{}_{Pt}$ at -50 mV vs. RHE was achieved, when the Pt electrode loading (0.9 μg_{Pt} $cm^{-2}{}_{geo}$) was optimized. This Pt mass activity is among the highest for Pt cluster and single-atom-based electrocatalysts reported so far. Hence our work demonstrates that ultrasmall and highly dispersed Pt entities, such as clusters and single atoms, deposited on MPNC nanospheres by a pCVD process are excellent electrocatalysts for the HER.

2. Results and Discussion

2.1. Effect of Pulse Number on MPNC-Pt-pCVD

Monodisperse MPNC nanospheres reported by us previously were used as a support material for the Pt deposition.[6,17,34,35] The synthesis of MPNC yielded nanospheres with a narrow particle size of 271 ± 29 nm, a pore size of 23 ± 3 nm, and a high degree of nitrogen doping (3.3 wt%) in agreement with our previous reports.[6,17,34,35] Further details of the MPNC characteristics can be found in Figures S1–S5, Table S3 (Supporting Information). The Pt-pCVD approach to MPNC was conducted in a fixed bed reactor with a custom-made receptable to contain an MPNC powder bed (Experimental Section and **Scheme 1**). In brief, the Pt organic precursor $MeCpPtMe_3$ was dosed for 1 s into a sealed

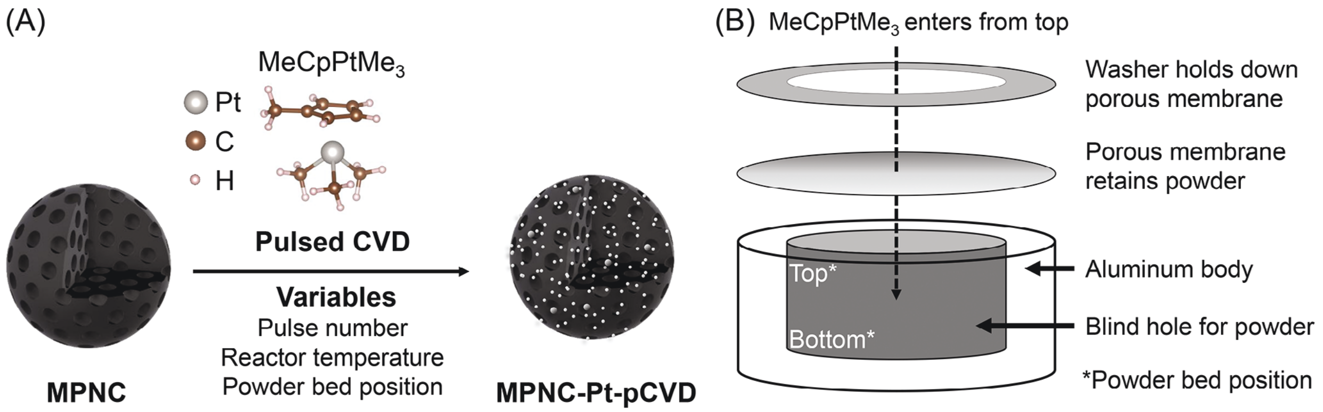

Scheme 1. A) Scheme[36] illustrating the pulsed CVD process for the synthesis of MPNC-Pt-pCVD in which a platinum precursor, MeCpPtMe$_3$, is pulsed and products are purged. B) Schematic of the receptacle used to retain the MPNC powder substrate during the deposition.

reactor and held for 30 s with inert N$_2$ gas flowing continuously. Thereby, the 30s dwell step provides time for MeCpPtMe$_3$ to infiltrate the MPNC powder bed and the MPNC pores. Then pumping of the chamber resumed, and the reactor was purged with N$_2$ for 10s.

To investigate the effect of Pt-pCVD pulse number on Pt loading, crystallinity, and dispersion on the synthesis of MPNC-Pt-pCVD materials, 50, 100, and 250 Pt-pCVD cycles were applied on MPNC at a constant temperature of 250 °C.

For the clarity of sample description, the following sample code is used: MPNC$_{A/C}$-Pt-pCVD-*X*-*Y*-T/B, where *X* is the number of applied Pt-pCVD pulses, *Y* is the temperature of the reaction chamber in °C, A or C is the amount of MPNC used in mg (A: 25 mg MPNC; C: 50 mg MPNC) and T/B is the sample position top or bottom in a fixed powder bed (Scheme 1), respectively.

The XRD patterns of MPNC$_A$-Pt-pCVD-X-250, top and bottom samples, are displayed in **Figure 1**A. The MPNC-related carbon phase shows specific reflections at 24.0° (002) and 43.7° (101), while the presence of additional reflections is found for

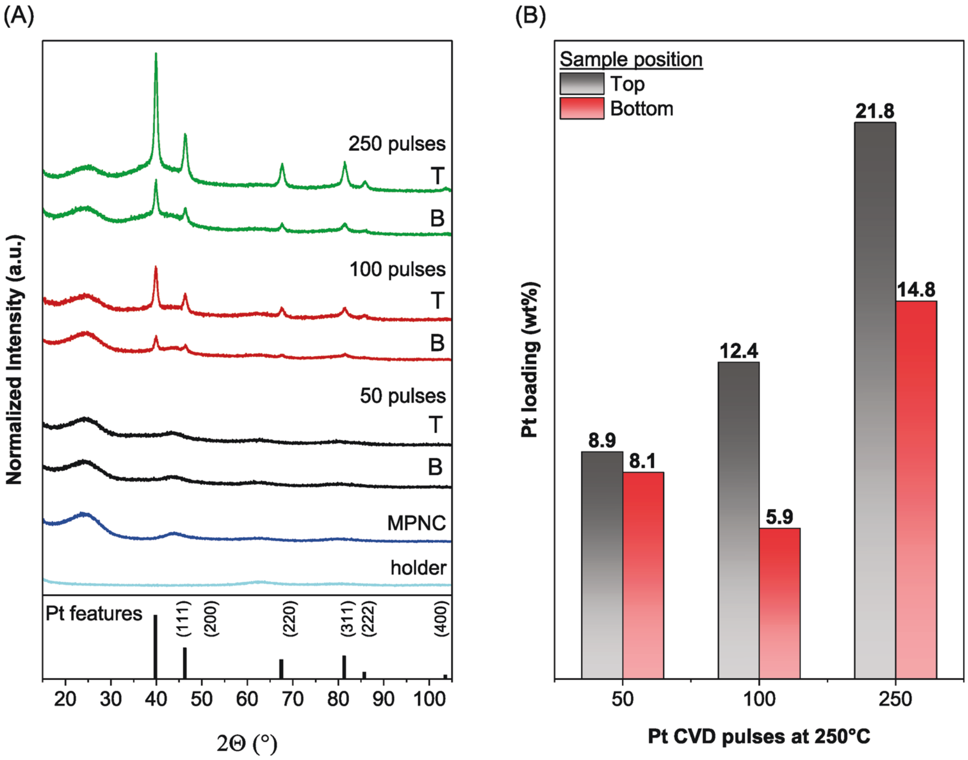

Figure 1. XRD of A) top T and bottom B samples of MPNC$_A$-Pt-pCVD-X-250 synthesized by applying X = 50, 100 and 250 Pt CVD pulses at 250 °C. The XRD pattern was normalized to the (002) carbon signal of pristine MPNC. B) Pt loading of MPNC$_A$-Pt-pCVD-X-250-T/B samples with varying numbers of pulses determined by TGA measurements.

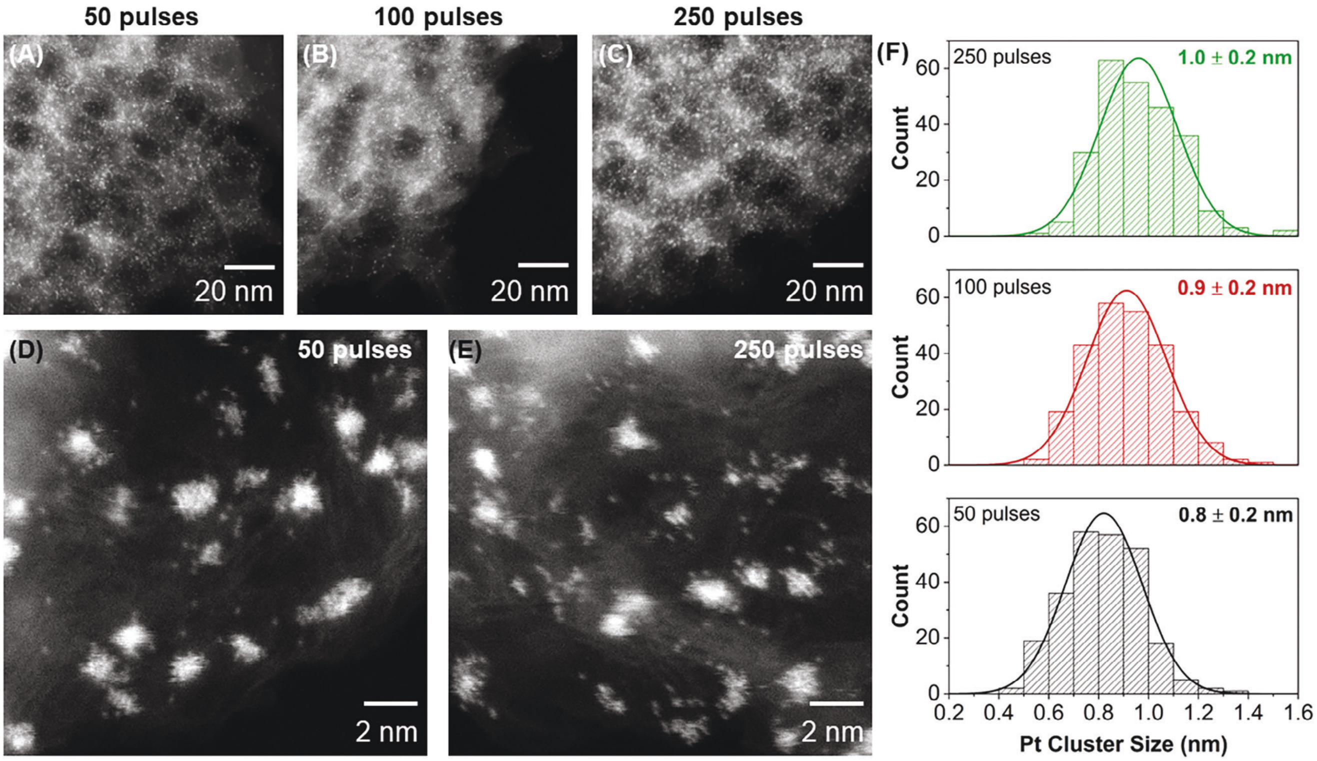

Figure 2. A–C) HAADF-STEM and D,E) ac-HAADF-STEM images of MPNC$_A$-pCVD-Pt-X-250-T reveal the presence of highly dispersed Pt clusters and single atoms. Top samples synthesized by applying $X = 50$, 100, and 250 Pt-pCVD pulses at a constant reactor temperature of 250 °C. F) Corresponding size distribution of Pt clusters.

crystalline Pt at 2Θ of 39.9°, 46.3°, 67.6°, 81.4°, 85.9° and 103.8° for samples synthesized with 100 and 250 Pt-pCVD pulses. The corresponding Pt *hkl* lattice planes are (111), (200), (220), (311) (222), and (400), respectively. The higher the number of pCVD pulses, the more intense the diffraction reflections are, though no reflexes are found for the MPNC$_A$-Pt-pCVD-50-250 top and bottom samples, which received the fewest pulses. A broad underlying signal is found for all samples in the 2Θ regions between ≈30° and ≈52°, in which the most intense Pt reflections for (111) and (200) are located at 39.9° and 46.3°. These results indicate the presence of Pt species with short-range ordering, while sharp reflections are attributed to crystalline Pt species.

Noteworthily, the intensity of the reflections for crystalline Pt is linked to the number of Pt-pCVD pulses for top and bottom samples with 100 and 250 pulses. However, the comparison between these top and bottom samples always revealed a lower intensity for bottom samples. As the intensity of the reflections depends on the occurrence of reflection-generating species, it can be deduced that the amount and/or the crystallinity of these crystalline Pt species found in top samples and samples with higher numbers of pulses is increased.[37] While it is assumed that the synthetic mechanism of Pt deposition at the top and bottom of the powder bed is identical, the powder at the top is exposed longer during each pulse creating a Pt gradient (with decreasing Pt concentration from the top of the powder bed to the bottom) due to the entering of the Pt precursor through the top of the receptacle and the time it takes for the precursor to penetrate the powder bed (Scheme 1B). Therefore, this Pt gradient leads to both an increased tendency to deposit/grow Pt species and elevated Pt loadings in the top portion of the powder bed. In fact, higher Pt loadings are always observed for top samples as measured by thermogravimetric analysis (TGA) (Figure 1B; Figure S6A,B, Supporting Information).

When the number of pulses increases, the Pt loading rises from 8.9 wt% for MPNC$_A$-Pt-pCVD-50-250-T to 21.8 wt% for MPNC$_A$-Pt-pCVD-250-250-T, and the disparity between top and bottom Pt loadings becomes larger, e.g., 10% for MPNC$_A$-Pt-pCVD-50-250 and 32% for MPNC$_A$-Pt-pCVD-250-250. This behavior may be assigned to the Pt gradient from each pulse and a catalyzing effect of Pt deposited in previous cycles accelerating the decomposition of the Pt precursor.[38,39]

In order to elucidate the morphology of Pt species with short-range and crystalline ordering, electron microscopy was applied. STEM micrographs of the top samples within the Pt-pCVD pulse study show highly and homogenously dispersed Pt clusters across the MPNC nanosphere surface and volume regardless of the number of pulse cycles (**Figure** 2A–C; Figure S7, Supporting Information). These clusters are assigned to the signal of short-range ordered Pt species as found by XRD. The high dispersion of Pt clusters is in line with the high and homogenous O- and N-distribution on/in the MPNC nanospheres leading to an optimized Pt precursor adsorption and dissociation (Figure S4, Supporting Information).[30,40] Moreover, by ac-HAADF-STEM imaging the presence of Pt single atoms on MPNC nanospheres is also observed, independent of the number of Pt-pCVD cycles (Figure 2D,E). These results are in good agreement with previous

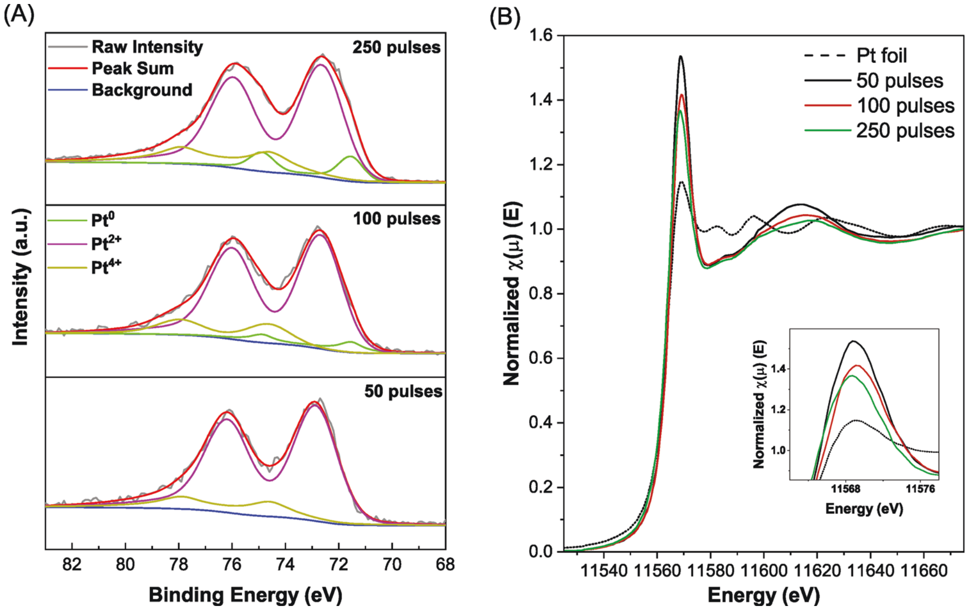

Figure 3. A) XPS fit of Pt4f and B) Pt L_3-edge XANES spectra of MPNC$_A$-Pt-pCVD samples as synthesized by applying respective 50, 100, and 250 Pt-pCVD cycles at a constant temperature of 250 °C.

literature on vapor deposition techniques reporting on the deposition of Pt clusters and/or single atoms on heteroatom-doped carbonaceous supports.[10,19,41,42]

The Pt cluster size distribution in Figure 2F revealed a cluster size of 0.8 ± 0.2, 0.9 ± 0.2, and 1.0 ± 0.2 nm for 50, 100, and 250 Pt-pCVD cycles, respectively. Although the standard deviation about the average value is relatively high (20–25%), and the difference between the average particle size of the samples is not very large, a trend toward larger entities with higher pulse numbers is evident and suggests a homogeneous Pt cluster growth during a pulse.

Subsequent to a thorough microscopic examination of the specimen revealing the dominant phase of Pt clusters and single atoms, larger Pt nanoparticles, and agglomerates were also observed in the MPNC$_A$-Pt-pCVD-250-250-T sample (Figure S8, Supporting Information). Therefore, crystalline Pt features in the XRD pattern as observed for MPNC materials treated with 100 and 250 Pt-pCVD cycles are assigned to these Pt species. On the basis of these findings, it can be deduced that growth or coalescence of larger Pt nanoparticles and agglomerates occurs at a critical number of pulses (or Pt loading). However, this effect was observed at a constant temperature of 250 °C and is dependent on temperature as presented in section 2.2. To demonstrate that similar Pt features are found on samples located at the bottom of the bed, MPNC$_A$-Pt-pCVD-250-250-B was microscopically investigated as an example for all samples (Figure S9, Supporting Information). TEM and HAADF-STEM micrographs exhibit a small Pt cluster size of 0.9 ± 0.2 nm, while larger Pt nanoparticles and agglomerates are barely found. The observed small difference in the Pt cluster size between top and bottom is one indicator for the lower Pt loading in the bottom samples.

The XPS Pt4f fitting of MPNC$_A$-Pt-pCVD top samples synthesized by applying 50, 100, and 250 Pt-pCVD cycles at 250 °C are shown in **Figure 3A**. Each Pt feature (Pt^0, Pt^{2+}, and Pt^{4+}) displays a double peak corresponding to Pt 4f$_{7/2}$ and Pt 4f$_{5/2}$ states due to spin-orbital coupling (Table S4, Supporting Information). Apart from MPNC$_A$-Pt-pCVD-50-250-T, Pt^0, Pt^{2+}, and Pt^{4+} are found for all samples in good agreement with Pt-based MPNC carbon materials reported previously, although the relative shares of each component are different as a result of the Pt species produced by the Pt-pCVD process.[6] The Pt4f fit of top and bottom portion of MPNC$_A$-Pt-pCVD-250-250 exhibits no significant changes (Figure S10B, Table S4, Supporting Information).

The samples are mostly composed of Pt^{2+} (>70%) and Pt^{4+} (>10%) as indicated in Table S4 (Supporting Information), which was also reported for similar Pt cluster- and single-atom-based samples.[42–44] While no Pt$^{\circ}$ feature could be found via XPS in MPNC$_A$-Pt-pCVD-50-250-T, the metallic contribution of Pt^0 in MPNC$_A$-Pt-pCVD samples synthesized by applying 100 and 250 Pt-pCVD cycles increased from 5.7% to 9.7%. Furthermore, the Pt^0 binding energy of 71.6 eV of these samples shows a slight shift to higher binding energies when compared to literature values of bulk Pt.[45,46] These observations may be due to the slight increase in Pt cluster size and occurrence of Pt nanoparticles and agglomerates from 50 to 250 Pt-pCVD cycles, as shown by XRD and STEM (Figures 1A, and 2; Figure S7, Supporting Information), since the binding energy of nanoparticles and clusters is governed by surface oxides and size.[45,47] Considering the high content of oxidized Pt of MPNC-Pt-pCVD samples, a sole assignment to surface oxides appears questionable. Single-site Pt is thought to be in the form of Pt^{2+}.[42] Therefore, we assign parts of the Pt^{2+} features to the high amount of Pt single sites on MPNC nanospheres also observed via ac-HAADF-STEM (Figure 2D,E).

In the XANES spectra the variation in the intensity of the white line at the Pt L_3-edge of MPNC$_A$-Pt-pCVD samples, which were subjected to varying numbers of Pt-pCVD pulses, was compared to a Pt foil, as a reference for Pt^0 (Figure 3B). A higher intensity of this white line suggests an increased average oxidation state

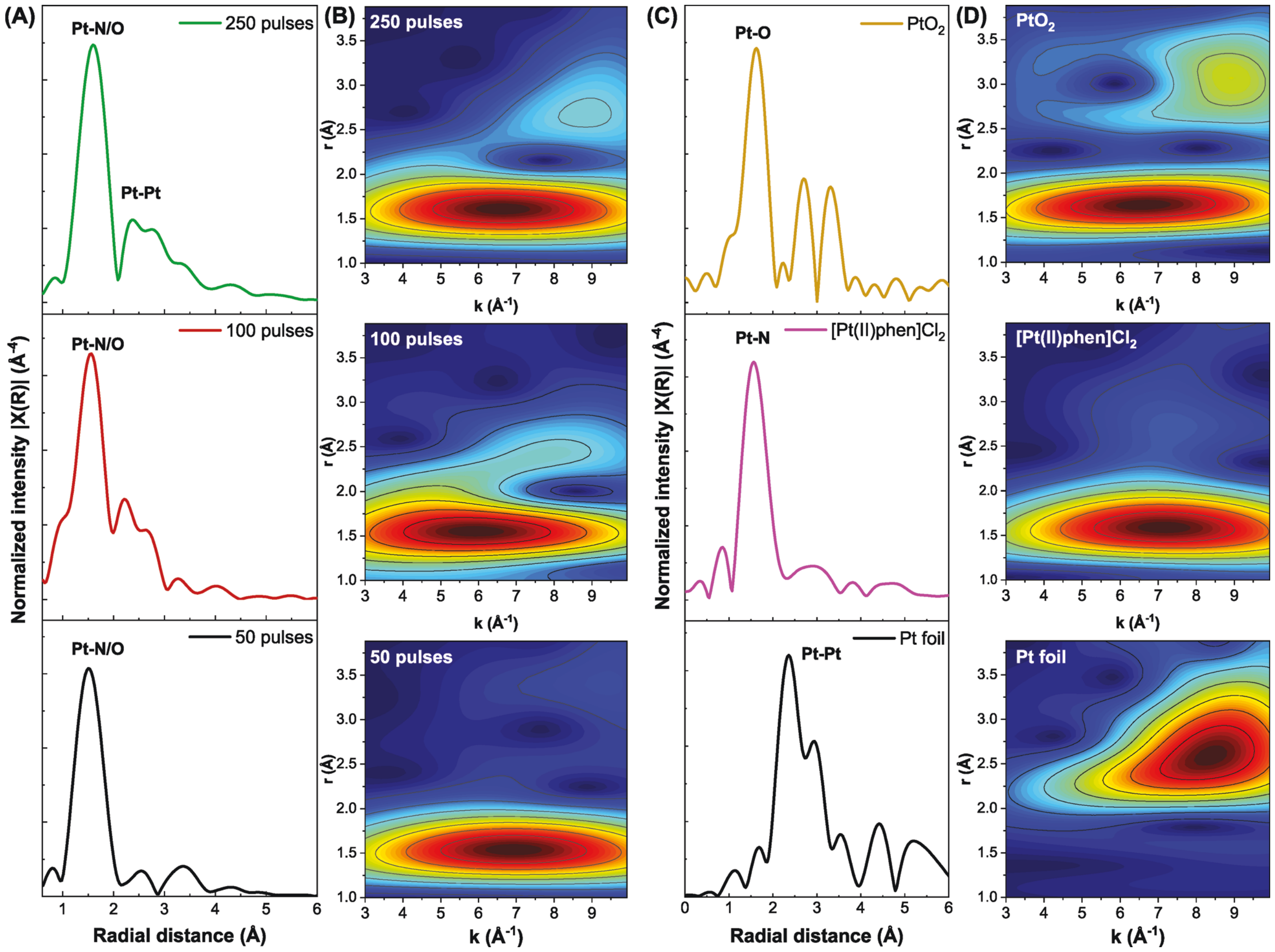

Figure 4. Comparison of (A, C) the Fourier-transform (FT) EXAFS Pt L_3-edge and (B, D) wavelet transform (WT)-EXAFS Pt L_3-edge spectra of MPNC$_A$-Pt-pCVD samples synthesized by applying respective 50, 100 and 250 Pt-pCVD cycles at a constant temperature of 250 °C and using Pt foil, Dichloro(1,10-phenanthroline)platinum(II) and PtO$_2$ as references.

(AOS) in the platinum sites.[6,48,49] The XANES spectra confirm the higher metallic character with increasing number of Pt deposition pulses since the intensity of the white line diminishes. The Pt L_3-edge arises due to dipole transitions from the $2p_{3/2}$ levels to the vacant $5d_{3/2}$, $5d_{5/2}$, and 6s states, primarily influenced by the $5d_{5/2}$ state. Given that the empty states just above the Fermi level predominantly exhibit 5d characteristics, the intensity of the white line is indicative of the presence of d-electron vacancies, allowing for the determination of platinum's oxidation state by using the calibration curve from known materials as reference (PtO$_2$, Dichloro(1,10-phenanthroline)platinum(II) ([Pt(II)phen]Cl$_2$), and Pt foil).[50,51] For analytical purposes, the spectra were analyzed by employing an arctangent step function to approximate the absorption edge and a pseudo-Voigt profile to characterize the white line peak with the derived calibration curve presented in Figure S11 (Supporting Information). The calculated AOS for each sample is shown in Figure S11B (Supporting Information). For example, as anticipated, the AOS of Pt decreases from 2.70 to 2.08 when the number of pulses is increased from 50 to 250. This observation suggests an enhancement in the metallic character of the Pt entities. The Fourier-transform (FT) EXAFS spectra show that as the number of pulses increases from 50 to 100 to 250, there is a prominent increase in the metallic character, as indicated by the intensification of peaks between 2–3 Å (**Figure** 4A). Moreover, the wavelet transform (WT) EXAFS analysis in Figure 4B reveals that with increasing number of pulses, a new local maximum appears at ≈2.6 Å, which is attributed to the scattering of the metallic cluster phase.

A dominant coordination shell situated at ≈1.5 Å in WT is observed which is attributed to either Pt—N or Pt—O coordination shells around the Pt center.[6,52,53] We proved this assignment by the analysis of FT and WT-EXAFS techniques of Dichloro(1,10-phenanthroline)platinum(II) and PtO$_2$ reference samples, showing maxima at ≈1.5 Å confirming the presence of a Pt-N/O coordination shell (Figure 4C,D). However, from an atomic perspective, these Pt-N/O signals can be attributed to both a superficially oxidized Pt surface of Pt clusters and nanoparticles and/or a high content of Pt single atoms located in the heteroatom-doped carbon matrix of MPNC nanospheres. This is in good agreement with EXAFS fitting. For both the MPNC$_A$-Pt-pCVD-50-250-T and MPNC$_A$-Pt-pCVD-250-250-T samples, the FT-EXAFS of the Pt L_3-edge was well-fitted to a mixed phase. These phases comprise Pt

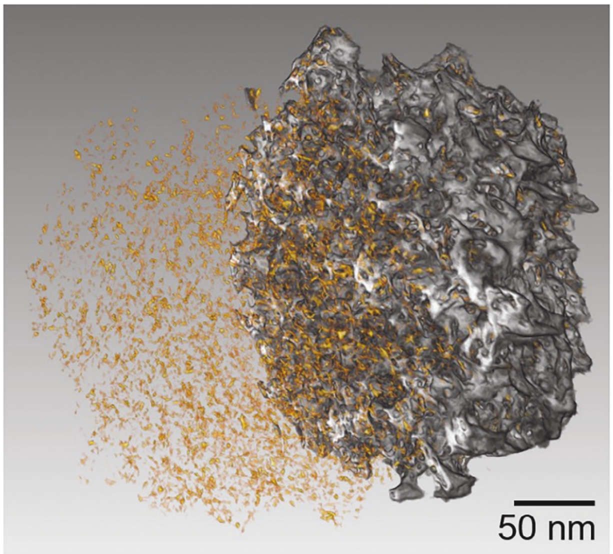

Figure 5. 3D tomography reconstructed image of MPNC$_C$-Pt-pCVD-250-250-T by STEM tomography. Golden fragments are platinum entities, while the darkish structure presents a half-cut MPNC nanosphere.

single atoms surrounded by Pt-N as the first coordination shells, along with Pt—O around ≈1.5–2.0 Å, and metallic Pt—Pt contributions ≈2.0–4.0 Å. The FT-EXAFS for the MPNC$_A$-Pt-pCVD-250-250-T sample specifically shows distinct Pt—Pt metallic coordination shells within the 2–4 Å range. This observation is attributed to the enhanced metallic character of the sample, which is a result of increasing the number of pulses (Figure S12, Tables S1 and S2, Supporting Information). However, although the ambiguity of the EXAFS interpretation cannot be resolved completely, it is clear from the combination of XRD, XPS, XAS, and electron microscopy methods that an ultra-high dispersion of Pt single atom centers is formed by the Pt-pCVD process.

To further elucidate the positioning of the Pt clusters and single atoms, a STEM-EDS line scan method (Figure S13, Supporting Information) and STEM tomography coupled with sections of EDS tomography were applied (**Figure 5**). The golden fragments in the 3D tomography reconstructed image in Figure 5 which represent platinum entities are located both on the outside and inside of the MPNC nanosphere, i.e., the pores within the mesoporous network. For better visibility of the MPNC nanosphere, represented in a darkish fashion, it is cut in half after the tomography reconstruction to probe the Pt distribution. Thereby, it is qualitatively obvious that Pt entities are distributed evenly throughout the 3D porous MPNC particle and that a shell structure is not apparent. In the Supporting Information, a drive-through movie segmented into carbon, platinum, and the combination of carbon and platinum is appended. The drive-through movie which is based on STEM tomography and EDS tomography sections (images on the left side in the movie) unambiguously displays first the highly porous and fully accessible network of MPNC nanospheres, second the ultra-small size of Pt entities and third the ultra-high dispersion of Pt entities throughout the whole nanosphere as well as the Pt positioning, which is mostly on the inside of the nanosphere within the porous network.

Considering the in-depth analysis of the effect of pulse number and fixed bed reactor geometry on MPNC-Pt-pCVD samples, it can be concluded that Pt cluster growth occurs by increasing the number of pulses, and a Pt gradient is created across the MPNC powder bed. While an ultra-high Pt dispersion is found for pCVD, the Pt gradient may be eliminated by using a fluidized bed reactor in order to create catalysts with homogenous Pt loadings. The concept of a fluidized bed reactor is well known.[18,22] For instance, highly dispersed Pt nanoparticles ranging from 1.5 to 3 nm supported on carbon with a Pt loading of ≈30 wt% were synthesized in a fluidized-bed ALD process with O_2 as a co-reactant.[4] However, such high Pt loadings with precise Pt speciation (clusters and/or single atoms) were not achieved by CVD processes using only N_2 as a carrier gas to the best of our knowledge.[9,10,30,32] Thus, our findings can help to exploit pCVD processes in a fluidized bed reactor in follow-up studies in order to adjust for example the Pt speciation under high Pt loadings even more precisely.

2.2. Effect of Temperature on MPNC-Pt-pCVD

After demonstrating that first the assignment of Pt entities is divided into larger Pt nanoparticles, clusters, and single sites, and second that with increasing pulses number the Pt loading and Pt cluster size in MPNC at 250 °C increases, the reaction temperature was varied to probe the impact on Pt loading, entities, crystallinity, and dispersion. For this purpose, the reactor was filled with 50 mg of MPNC, and 250 Pt-pCVD pulses were performed at 225, 250, and 300 °C (MPNC$_C$-Pt-pCVD-250-Y-T/B; C: 50 mg of MPNC used in the reactor, *Y* in °C, T/B top or bottom sample, respectively).

The analysis of XRD (Figure S14A, Supporting Information), TGA (Figures S6C,D and S14B, Supporting Information), STEM (Figure S15, Supporting Information), XPS (Figure S16, Table S5, Supporting Information) and XAS (Figure S17, Supporting Information) revealed the following characteristics of MPNC-Pt-pCVD samples treated at different temperatures: 1) Pt clusters and single atoms are detectable for all samples with a negligible amount of Pt nanoparticles/agglomerates for samples treated at 250 °C and 300 °C; 2) Pt clusters have the sizes of 1.0 ± 0.2 nm for MPNC$_C$-Pt-pCVD-250-225-T and MPNC$_C$-Pt-pCVD-250-250-T and 1.2 ± 0.3 nm for MPNC$_C$-Pt-pCVD-250-300-T; 3) At the reaction temperature of 250 °C, the largest amount of Pt nanoparticles and agglomerates are generated, while their amount at 300 °C is smaller; 4) Bottom samples generally show lower Pt loadings, as a result of a Pt precursor gradient across the fixed powder bed.

The particular results of the temperature-dependent Pt-pCVD on MPNC nanospheres as found by the aforementioned techniques lie in the thermal stability and decomposition process of the MeCpPtMe$_3$ precursor. For instance, an unexpectedly low Pt loading of only 0.9 wt% was found for the bottom sample MPNC$_C$-Pt-pCVD-250-300. Setthapun et al. observed a strong tendency of MeCpPtMe$_3$ to decompose at elevated temperatures, and 300 °C tends to be an upper-temperature limit for thermal ALD processes with this precursor.[24] Even at 100 °C they found that 10–15% of the MeCpPtMe$_3$ is reduced during the first adsorption step on their oxide support and during a N_2 purge at

300 °C for 40 min, 90% of the adsorbed Pt precursor thermally decomposed in the absence of reactive gases. Furthermore, metallic Pt films were observed on the sample holder and the quartz reactor tube at this temperature.

In contrast, Mulders et al. demonstrated no decomposition of $MeCpPtMe_3$ at 360 °C on a native Si oxide under vacuum in an electron microscope.[54] Kim et al. observed the formation of small nanoparticles in the range of 1–2 nm on carbon supports via CVD of Pt.[30,32] They used a constant $MeCpPtMe_3$ exposure in an N_2 atmosphere across a range of deposition temperatures and noted that the increase in Pt loading correlated with an increased Pt precursor decomposition due to elevated temperature. A steady increase of Pt loading between 140 and 300 °C is observed. Presumably, more nanoparticles of the same size are formed rather than nanoparticle growth. However, neither the size distribution of the Pt particles nor a complete XRD analysis was provided. Hence, the thermal decomposition of the precursor and Pt deposition are strongly dependent on interacting parameters such as the substrate, exposure time, gas type, and pressure. We suspect that the kinetics of $MeCpPtMe_3$ decomposition at 300 °C in our own experiment may be so rapid that once a surface is contacted, be it the sample or parts of the reactor, deposition occurs. This results in a slight increase in Pt cluster size and broadened size distribution (Figure S15C, Supporting Information), enhanced decomposition of the precursor on the reactor walls and membrane during the Pt-pCVD cycle, and extended exposure of the top of the bed with the precursor compared to the bottom portion. It has to be added to this point that a further conceivable explanation for this partial presence of Pt nanoparticles and agglomerates may be a temperature-driven partial coalescence of Pt. By comparing samples treated at temperatures <300 °C, the Pt deposition with respect to Pt loading is found to be optimal at 250 °C (16.2 wt%). Hence, while the Pt precursor decomposition is too fast at 300 °C yielding increased coating of reactor walls, it is too slow at 225 °C resulting in a considerable removal of Pt precursor via the pumping system. However, in terms of Pt speciation, the most controlled synthesis can be conducted using 225 °C as no larger Pt nanoparticles and agglomerates are found.

To further investigate the ultrasmall and highly-dispersed Pt clusters and single atoms, we employed electrochemical CV and CO stripping and used a Pt nanoparticle-based uniform, commercial Pt/C electrocatalyst (HiSPEC3000, 20 wt% of Pt on Vulcan XC72R) for reference. The full characterization of this electrocatalyst was shown elsewhere.[6] The Pt nanoparticles of this electrocatalyst are supported on commercial polydisperse carbon particles in the range of ≈20–80 nm, while the Pt crystallite size and particle size are 2.4 and 2.9 ± 0.6 nm as determined by XRD and TEM, respectively.

All samples exhibit typical features of Pt in acidic electrolytes in their cyclic voltammograms such as hydrogen underpotential deposition (H_{upd}) and Pt oxidation and PtO/OH reduction (Pt ox/red), though differences between the electrocatalysts are observed (**Figure** 6A). While $MPNC_C$-Pt-pCVD-250-225-T and $MPNC_C$-Pt-pCVD-250-300-T only show broad peaks for H_{upd} and Pt ox/red, more distinct peaks appear for $MPNC_C$-Pt-pCVD-250-250-T and Pt/C.

From single-crystal experiments, it is known that these signals arise from crystalline facets and are more pronounced the more crystalline the samples are.[55–57] Thus, these findings indicate from this perspective a more crystalline structure of the samples treated at 250 °C and Pt/C when compared to samples treated at 225 and 300 °C. Indeed, as shown by XRD, $MPNC_C$-Pt-pCVD-250-250-T, and Pt/C exhibit the most intense reflections for the Pt fcc phase which is attributed to Pt nanoparticles and agglomerates (Figure S14A, Supporting Information and[6]). In the case of the $MPNC_C$-Pt-pCVD top sample treated with 250 pulses at 300 °C, the CV result suggests a very low abundancy of these crystalline Pt species due to the absence of distinct H_{upd} features. This finding is in line with the XRD findings (Figure S14A, Supporting Information).

Then, CO stripping experiments were performed to gain further insight into the Pt speciation of the $MPNC_C$-Pt-pCVD samples treated at different temperatures (Figure 6B). Thereby, a 0.1 M $HClO_4$ electrolyte was used in order to avoid anion adsorption of the electrolyte on the electrocatalyst throughout the experiment.[58] After a chronoamperometric potential hold at 0.1 V vs. RHE under CO saturation, cyclic voltammograms between 1.2 and 0.05 V vs. RHE under N_2 saturation were recorded. The first cycle depicts the CO oxidation peaks for all electrocatalysts investigated, whereas no CO oxidation was found during the second cycle (dashed line) confirming that only surface-adsorbed CO is oxidized. The main peak maxima are found at 805 ± 6, 861 ± 3, 875 ± 2, and 888 ± 2 mV vs. RHE and follow the order from the lowest to the highest potential for Pt/C, $MPNC_C$-Pt-pCVD-250-250-T, $MPNC_C$-Pt-pCVD-250-300-T and $MPNC_C$-Pt-pCVD-250-225-T. Although the CO oxidation peak position may be sensitive to various factors such as particle size, faceting, loading, measurement protocol, etc., we assume that particle size which directs adsorption energies of reactants involved in the CO oxidation plays a major role in the peak positioning.[6,59] Furthermore, it has been reported previously that the CO oxidation peak shifts to lower potentials for larger Pt species, in particular nanoparticles.[6,59] Thus, these peak maxima are attributed to the major Pt species present in the corresponding samples. This means that Pt clusters found for $MPNC_C$-Pt-pCVD samples exhibit a CO oxidation peak maximum at potentials >860 mV vs. RHE, while Pt nanoparticles as determined for Pt/C display a maximum at 805 ± 6 mV vs. RHE. Based on this basic classification, the question now arises whether the other Pt species, i.e., agglomerates and single atoms, are also active/sensitive in/to CO stripping. Figure 6C therefore shows a background corrected zoom-in of the relevant CO oxidation range. This potential range was subdivided into 4 sections with limits of 740, 817, and 1022 mV vs. RHE. In the first section below 740 mV vs. RHE, signals are found for Pt/C, $MPNC_C$-Pt-pCVD-250-250-T, and $MPNC_C$-Pt-pCVD-250-300-T, which are assigned to larger Pt nanoparticles or agglomerates as shown by a previous review publication.[59] Noteworthily, the intensities of these signals are in line with diffraction intensities (Figure S14A, Supporting Information) and CV-based H_{upd} features (Figure 6A) of $MPNC_C$-Pt-pCVD-250-250-T and $MPNC_C$-Pt-pCVD-250-300-T. Although the separation between Sections 2 and 3, Figure 6C is not arbitrarily sharp, as suggested here by the separation line at 817 mV vs. RHE, isolated Pt nanoparticles larger than ≈2 nm can be assigned to sections 2, Figure 6C.[60] This assignment illustrates well the Pt speciation and the relative qualitative abundance of these species in Pt/C, $MPNC_C$-Pt-pCVD-250-250-T and

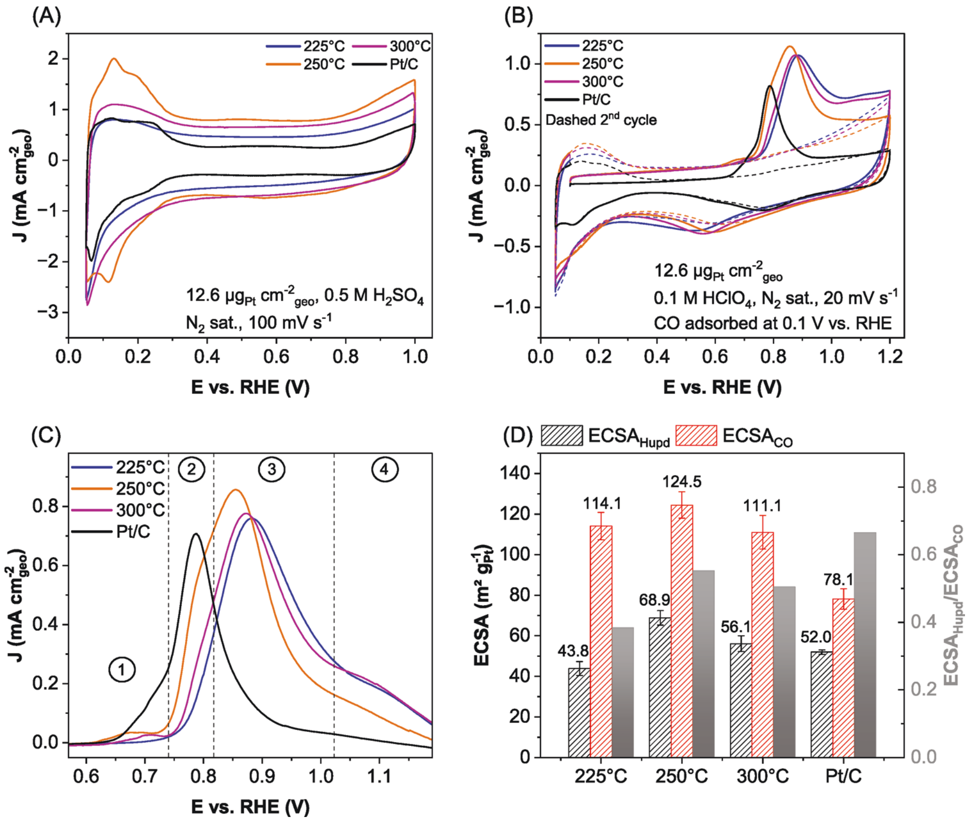

Figure 6. A) Cyclic voltammetry, B) CO stripping, C) background corrected zoom-in of CO stripping, and D) corresponding ECSA values of MPNC$_C$ top samples with constant 250 Pt-pCVD pulses at 225, 250, 300 °C and commercial Pt/C electrocatalyst. Electrochemical details are provided in the figures.

MPNC$_C$-Pt-pCVD-250-300-T (Figures S14A; Figure S15, Supporting Information and[6]), since Pt/C, MPNC$_C$-Pt-pCVD-250-250-T and MPNC$_C$-Pt-pCVD-250-300-T show a clear peak, a prominent peak shoulder and a small peak shoulder in this potential range, respectively. Sections 3, Figure 6C displays the peak maxima of MPNC$_C$-Pt-pCVD samples standing for ultrasmall Pt clusters as mentioned above. Interestingly, the potentials of the peak maxima follow the order of MPNC$_C$-Pt-pCVD-250-225-T > MPNC$_C$-Pt-pCVD-250-300-T > MPNC$_C$-Pt-pCVD-250-250-T which could be correlated to a slight size effect within the sample set (Figure S15). While MPNC$_C$-Pt-pCVD-250-300-T exhibits a Pt cluster size of 1.2 ± 0.3 nm, MPNC$_C$-Pt-pCVD-250-225-T possesses 1.0 ± 0.2 nm sized Pt clusters following this rational. In contrast, Pt clusters of MPNC$_C$-Pt-pCVD-250-250-T are also in the range of 1.0 ± 0.2 nm but show a lower CO oxidation potential when compared to the other Pt-pCVD-based samples. This finding could possibly be explained by a size effect, which is based on the assumption that the growth of Pt entities occurs at 250 °C (see section 2.2.). Thus, it is assumed that the distribution of Pt cluster sizes of MPNC$_C$-Pt-pCVD-250-250-T includes small fractions of particles between ≈1-2 nm that are not observed by the limited and locally orientated microcopy-based analysis.

In, section 4, Figure 6C above a potential of 1022 mV vs. RHE pronounced peaks are only found for MPNC$_C$-Pt-pCVD samples which are hypothesized to show CO oxidation on Pt single atoms. Due to synthetic challenges to access high Pt loadings of purely Pt single sites on carbon supports, research is not able to investigate CO oxidation and mechanism on carbon-supported Pt single-atom electrocatalysts. However, some works pointed to the existence of electrochemical CO oxidation on carbon-supported Pt single-atom based electrocatalysts consisting of solely Pt single atoms or of mixtures of Pt nanoparticles, clusters, and single atoms, as they found significant contribution to a CO oxidation peak at ≈1 V vs. RHE of a carbon-supported Pt single-atom electrocatalyst.[6,44,61]

Hence, our result of electrochemical CO stripping on MPNC$_C$-Pt-pCVD consisting of high Pt loading and high abundancy of Pt single atoms as determined by TGA, ac-HAADF-STEM, XPS, and XAS could be another piece of the puzzle in the research of electrochemical CO oxidation on carbon-supported Pt single atoms and in general Pt electrocatalysts. In addition, if further works with systematic and clear electrochemical measurement protocols could confirm these findings on highly loaded and pure Pt single-atom carbon samples, the electrochemical CO oxidation may become a powerful analytical tool for Pt single-atom determination without the use of expensive facilities/instruments such as a synchrotron or an aberration-corrected STEM.

The electrochemical active surface area (ECSA) for H$_{upd}$ and CO stripping was calculated based on Equation S1, (Supporting Information) and revealed the highest ECSA for MPNC$_C$-Pt-pCVD-250-250-T (ECSA$_{Hupd}$: 69 ± 4 m^2 g^{-1}$_{Pt}$; ECSA$_{CO}$: 125 ± 6 m^2 g^{-1}$_{Pt}$) as shown in Figure 6D. In contrast, the reference electrocatalyst Pt/C only possesses an ECSA$_{Hupd}$ of 52 ± 1 m^2 g^{-1}$_{Pt}$ and ECSA$_{CO}$ of 78 ± 5 m^2 g^{-1}$_{Pt}$. The enhanced ECSA val-

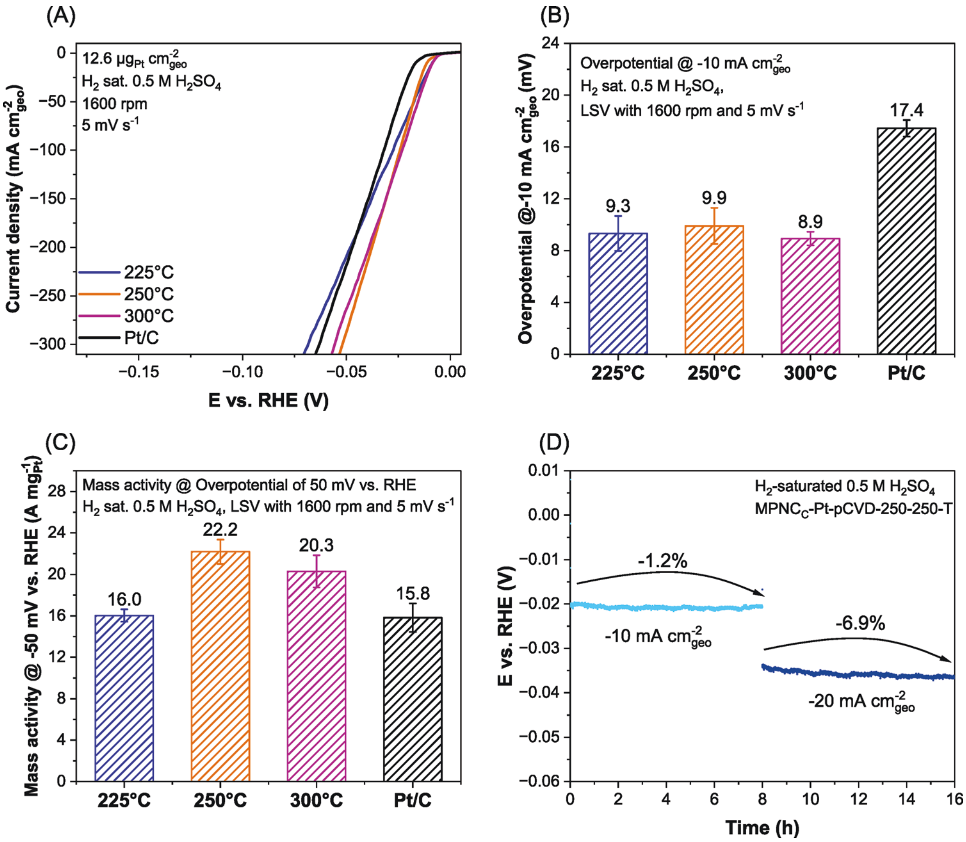

Figure 7. A) Geometric current density of MPNC$_C$ top samples with constant 250 Pt pCVD pulses at 225, 250, and 300 °C and Pt/C reference electrocatalyst in H_2 saturated 0.5 м H_2SO_4 under 1600 rpm and 5 mV s^{-1} sweep rate with a constant Pt electrode loading of 12.6 μg$_{Pt}$ cm$^{-2}_{geo}$. B) Overpotential at -10 mA cm$^{-2}_{geo}$ and Pt mass activity at an overpotential of 50 mV vs. RHE of MPNC$_C$ top samples with constant 250 Pt pCVD pulse at 225, 250 and 300 °C and Pt/C reference electrocatalyst. Chronopotentiometric stability test of MPNC$_C$-Pt-pCVD-250-250-T at -10 mA cm$^{-2}_{geo}$ and -20 mA cm$^{-2}_{geo}$ for 8 h, respectively.

ues of the Pt-pCVD-based samples are due to the ultrasmall and highly dispersed Pt entities found on the MPNC nanospheres. Furthermore, the ratio of ECSA$_{Hupd}$ to ECSA$_{CO}$ (Figure 6D) was calculated and demonstrated lower values for MPNC$_C$-Pt-pCVD in comparison to Pt/C and points to the existence of Pt clusters since multiple CO oxidation on Pt entities, e.g., clusters, were postulated in previous works.[6,61]

The relative differences between the ECSA values within the study may be attributed to an enhanced Pt deposition process at 250 C (Pt loading: 16.2 wt% of MPNC$_C$-Pt-pCVD-250-250-T versus 9.3 wt% for MPNC$_C$-Pt-pCVD-250-225-T and 10.5 wt% for MPNC$_C$-Pt-pCVD-250-300-T) which may allow for an increased Pt nuclei formation resulting in increased Pt dispersion. Presumably, this elevated dispersion compensates for the ECSA loss due to larger Pt nanoparticles and agglomerates (Figure S14A, Supporting Information).

2.3. HER Electrocatalysis of MPNC-Pt-pCVD

After in-depth material characterization of the resulting MPNC$_C$-Pt-pCVD, which revealed the presence of ultra-highly dispersed Pt clusters and single atoms with negligible amounts of nanoparticles and agglomerates for a few samples, the electrocatalytic activities for the HER of MPNC$_C$-Pt-pCVD-250-225-T, MPNC$_C$-Pt-pCVD-250-250-T and MPNC$_C$-Pt-pCVD-250-300-T electrocatalysts were tested and compared with a commercial Pt/C electrocatalyst. Thereby, the electrochemical analysis was conducted with the same Pt electrode loading (12.6 μg$_{Pt}$ cm$^{-2}_{geo}$) of the electrocatalysts in H_2-saturated 0.5 м H_2SO_4 by linear sweep voltammetry (LSV) using a three-electrode rotating disk electrode (RDE) system. Further details can be found in the experimental section.

In electrochemical water electrolysis, geometric current density, i.e., mA cm$^{-2}_{geo}$, and Pt mass activity, i.e., A mg$^{-1}_{Pt}$, play important roles in reducing the cost for broad commercialization for PEMWE systems. The investigated Pt-pCVD-based electrocatalysts exhibit high geometric current density over the entire overpotential voltage range as shown in **Figure 7A** due to the advantageous Pt entities generated by the pCVD process. While up to an overpotential of ≈15 mV vs. RHE, MPNC$_C$-Pt-pCVD-250-225-T, and MPNC$_C$-Pt-pCVD-250-300-T have higher geometric current density, at overpotentials > 30 mV vs. RHE, MPNC$_C$-Pt-pCVD-250-250-T shows higher geometric current densities. Remarkably, all electrocatalysts prepared by Pt-pCVD performed equally better in a small current density regime (-10 mA cm$^{-2}_{geo}$) as reflected by the lower overpotentials of 9.3 ± 1.3, 9.9 ± 1.4, 8.9 ± 0.5 mV vs. RHE for respectively MPNC$_C$-Pt-pCVD-250-225-T, MPNC$_C$-Pt-pCVD-250-250-T and MPNC$_C$-Pt-pCVD-

250-300-T compared to the reference electrocatalyst with 17.4 ± 0.6 mV vs. RHE. Within the temperature series, the differences are marginal when based on the overpotential (Figure 7B). However, they follow the order of MPNC$_C$-Pt-pCVD-250-225-T ~ MPNC$_C$-Pt-pCVD-250-300-T < MPNC$_C$-Pt-pCVD-250-250-T << Pt/C and thus correspond to the potentiostatic impedance spectra at -10 mV vs. RHE, where the smallest charge transfer resistances (R_{ct}), represented by the smallest second semicircles in the Nyquist plot, are found for samples MPNC$_C$-Pt-pCVD-250-225-T ~ MPNC$_C$-Pt-pCVD-250-300-T and the largest R_{ct} for the reference electrocatalyst (Figure S18, Supporting Information). This indicates that electron transfer within the HER requires lower energy to be expended for the Pt-pCVD-prepared electrocatalysts compared to the reference, resulting in an increase in activity for low overpotentials/current densities.[62] When the R_{ct} values are correlated with ECSA values, a dependence is found by comparing the MPNC-Pt-pCVD samples with the reference electrocatalyst ($ECSA_{MPNC\text{-}Pt\text{-}pCVD} > ECSA_{Pt/C}$ and $R_{ct,MPNC\text{-}Pt\text{-}pCVD} < R_{ct,Pt/C}$). However, within the MPNC-Pt-pCVD sample set, an exactly opposite relationship is shown ($ECSA_{MPNC\text{-}C\text{-}Pt\text{-}pCVD\text{-}250\text{-}225/300\text{-}T} < ECSA_{MPNC\text{-}C\text{-}Pt\text{-}pCVD\text{-}250\text{-}250\text{-}T}$ and $R_{ct,MPNC\text{-}C\text{-}Pt\text{-}pCVD\text{-}250\text{-}225/300\text{-}T} < R_{ct,MPNC\text{-}C\text{-}Pt\text{-}pCVD\text{-}250\text{-}250\text{-}T}$). This may be attributed to the slightly different Pt speciation of MPNC$_C$-Pt-pCVD-250-250-T as illustrated by CV-based H_{upd} and CO stripping measurements (Figure 6A,B). We therefore suggest, on the basis of our findings that there is among other effects a size[63] and interacting effect[53] of different Pt entities in the small current density range, which should be further investigated by follow-up studies.

At higher current densities, the effect of mass transport of protons and H_2 plays a larger role. Due to the very efficient HER process, the removal of H_2 from active sites and the provision of protons through the electrode is pivotal. Thus, for increased HER performance at higher current densities an ultra-high dispersion of Pt should be paired with thin electrode structuring.[6] In fact, the current density of MPNC$_C$-Pt-pCVD-250-250-T (282 ± 14 mA cm^{-2}_{geo} at -50 mV vs. RHE) with the highest Pt loading of 16.2 wt% of primarily Pt clusters, single atoms and negligible amounts of nanoparticles and agglomerates (Figures S14B and S15, Supporting Information and Pt speciation analogue to sample presented in Figure 2E; Figure S8, Supporting Information), leading to the thinnest electrode at the same absolute Pt electrode loading of 12.6 μg_{Pt} cm^{-2}_{geo} among the Pt-pCVD samples (Figure S19, Supporting Information), outperforms MPNC$_C$-Pt-pCVD-250 top sample treated at 225 °C (202 ± 7 mA cm^{-2}_{geo}) and 300 °C (255 ± 20 mA cm^{-2}_{geo}). This trend is also found for high current densities in the range between 300–500 mA cm^{-2}_{geo} and when the current is normalized to the Pt electrode loading of the Pt-pCVD electrocatalysts (Figure S19, Supporting Information). For instance, the Pt mass activity of MPNC$_C$-Pt-pCVD-250-250-T of 22 ± 1 A mg^{-1}_{Pt} at an overpotential of 50 mV vs. RHE is 38% and 9% higher than the corresponding electrocatalysts at Pt-pCVD temperature of 225 °C (16 ± 1 A mg^{-1}_{Pt}) and 300 °C (20 ± 2 A mg^{-1}_{Pt}), respectively (shown in Figure 7C). When the Pt mass activity of MPNC$_C$-Pt-pCVD-250-250-T electrocatalyst (22 ± 1 A mg^{-1}_{Pt}) is compared to the reference electrocatalyst Pt/C (16 ± 1 A mg^{-1}_{Pt}) at -50 mV vs. RHE, a 40% increase in HER performance is observed which we attribute to the large ECSA ($ECSA_{Hupd}$: 69 ± 4 m^2 g^{-1}_{Pt}; $ECSA_{CO}$: 125 ± 6 m^2 g^{-1}_{Pt} for MPNC$_C$-Pt-pCVD-250-250-T versus $ECSA_{Hupd}$: 52 ± 1 m^2 g^{-1}_{Pt}; $ECSA_{CO}$: 78 ± 5 m^2 g^{-1}_{Pt} for Pt/C) of the MPNC$_C$-Pt-pCVD-250-250-T originated by ultra-high Pt dispersion of Pt entities. Hence, Pt utilization is substantially increased by the Pt-pCVD process on MPNC nanospheres under the same electrode loading in comparison to the reference electrocatalyst.

Regarding the HER mechanism in the acid electrolyte on Pt, three fundamental steps are involved, namely, i) Volmer step: $H_3O^+ + e^- \rightarrow H_{ads} + H_2O$, ii) Heyrovsky step: $H_{ads} + H_3O^+ + e^- \rightarrow H_2 + H_2O$ and iii) Tafel step: $H_{ads} + H_{ads} \rightarrow H_2$.[64] Previous studies have elaborated with a combined approach of Tafel slope analysis and the use of density functional theory that Pt-based electrocatalysts involving adjacent Pt sites as found in Pt nanoparticles/clusters or Pt single atoms in close proximity to Pt clusters preferably follow the Volmer-Tafel pathway,[41,53] while purely Pt single-atom electrocatalysts conduct the HER mechanism by either the Volmer-Heyrovsky[42,43] or the Volmer-Tafel[19] reaction path in acidic electrolyte. Thus, the elucidation of the HER mechanism of Pt single atoms is still under investigation. However, on the basis of the aforementioned literature of HER reaction pathways, it can be assumed that the Volmer-Tafel type reaction is the primary HER mechanism for this MPNC-Pt-pCVD electrocatalyst.

In addition to the excellent geometric and Pt mass activity and low electrochemical R_{ct}, the MPNC$_C$-Pt-pCVD-250-250-T electrocatalyst also exhibited good stability, as shown in Figure 7D. The chronopotentiometric HER test was performed at two constant current densities (−10 and -20 mA cm^{-2}_{geo}) for 8 h each. In each case, the overpotential decreased by only 1.2% at −10 mA cm^{-2}_{geo} and by only 6.8% at −20 mA cm^{-2}_{geo} for 8 h of continuous operation.

In our previous study on wet-chemical Pt deposition and gaseous chemical reduction of Pt on MPNC nanospheres, we found a strong dependence of the Pt electrode loading on the electrochemical HER activity of the Pt/MPNC electrocatalyst.[6] This dependency was now also demonstrated for MPNC$_C$-Pt-pCVD-250-250-T (Figure S20A–D, Supporting Information). As mentioned above, due to the mass transport of H_2 facilitated by thinner electrodes, i.e., lower geometrical Pt loading, the current density normalized to the mass of catalyst (Pt and carbon mass), i.e., A mg^{-1}_{Cat}, and Pt mass, i.e., A mg^{-1}_{Pt}, increases at lower Pt electrode loading (25.4, 12.6, 6.4, 0.9 μg_{Pt} cm^{-2}_{geo}), whereas the absolute current density normalized to geometric electrode surface area, i.e., mA cm^{-2}_{geo}, decreases with low Pt electrode loading (Figure S20A–C, Supporting Information). Since Pt is a highly active electrocatalyst for the electrochemical conversion of protons to hydrogen, and the resulting hydrogen blocks catalytically active sites, mass transport of hydrogen (bubbles) is a limiting factor.[65] For example, the Pt or catalyst mass activity increases by a factor of ≈4.4 at an overpotential of 50 mV vs. RHE due to the reduction of the Pt electrode loading (from respectively 25.4 μg_{Pt} cm^{-2}_{geo} to 0.9 μg_{Pt} cm^{-2}_{geo}) from 12.8 ± 0.4 to 56 ± 2 A mg^{-1}_{Pt} and from 2.1 ± 0.1 to 9.1 ± 0.4 A mg^{-1}_{Cat} (Figure S20D, Supporting Information). Compared with the above-mentioned Pt-based nanoparticle, cluster, and single atom electrocatalysts Pt-IWI/MPNC, we found a similar Pt mass activity of 56 ± 2 A mg^{-1}_{Pt} (at -50 mV vs. RHE) at low Pt electrode loading of 0.9 μg_{Pt} cm^{-2}_{geo}, which we qualitatively attribute to the presence of primarily Pt clusters and Pt single atoms (Figure S20E, Supporting Information). Remarkably, the catalyst mass activity of MPNC$_C$-Pt-pCVD-250-250-T of 9.1 ± 0.4 A mg^{-1}$_{Cat}$, was ≈20% lower than the reference value of Pt-IWI/MPNC, which we again relate to the thinner electrode layer as a result of the higher Pt content in Pt-IWI/MPNC (20 wt%) versus MPNC$_C$-Pt-pCVD-250-250-T (16.2 wt%). These results and the comparison with state-of-the-art Pt cluster and single-atom based HER electrocatalysts shown in Figure S20E, (Supporting Information), which have significantly lower Pt loadings (1-2 wt%), demonstrate the need for high Pt loadings with controllable Pt speciation, for setting high ECSA values and optimized mass transport through tailored electrodes. In summary, the advantageous pCVD process presented herein makes it possible to increase Pt loading while generating access to ultra-highly dispersed Pt clusters and single atoms on an MPNC nanosphere support material. By understanding and controlling the Pt deposition process by Pt-pCVD, the best MPNC-based Pt-pCVD electrocatalyst showed an ultra-high Pt HER mass activity of 56 ± 2 A mg^{-1}$_{Pt}$ at -50 mV vs. RHE, which is among the best Pt single-atom and cluster-based Pt mass activities to date.[41,53,66]

3. Conclusion

In this study, we presented ultrasmall and highly dispersed Pt (sub) nanometer-sized clusters and single atoms on a high-surface-area, monodisperse MPNC nanosphere support material with improved HER performance. The Pt entities were deposited by a pCVD approach on the MPNC powder supports. The process involves the volatile Pt precursor MeCpPtMe$_3$, carried by nitrogen gas using an adjustable number of pulses and temperature. Comprehensive in-depth material characterization including XRD, STEM-EDS tomography, ac-HAADF-STEM, TGA, XPS, XAS, and electrochemical CO stripping was applied to elucidate the nature and dispersion of the deposited Pt entities. The developed Pt-pCVD process led to an exceptional dispersion of Pt clusters, with an average size of ≈1 nm and the presence of single atoms on the MPNC supports. Interestingly, under specific conditions, a limited number of Pt nanoparticles and agglomerates were also formed due to reactor geometry and the kinetics of precursor decomposition. It was observed that increasing the number of Pt-pCVD cycles to 250 slightly augmented the size of the Pt clusters, particularly at a high Pt loading of 21.8 wt%.

Our findings indicate that temperature- and surface-controlled precursor decomposition enables the sole presence of Pt clusters and single atoms at temperatures of 225 °C by using this Pt-pCVD approach. By understanding the dependencies related to temperature, pulse frequency, and reactor design, we achieved targeted Pt species and ultra-high Pt dispersion across the MPNC nanosphere support. The electrochemical HER performance of the MPNC-Pt-pCVD samples using deposition temperatures of 225, 250, and 300 °C was further evaluated and benchmarked against a commercial Pt/C reference electrocatalyst. Due to the high Pt dispersion (in the form of clusters and single sites) an ultrahigh ECSA$_{CO}$ of > 110 m^2 g^{-1}$_{Pt}$ for MPNC-Pt-pCVD samples is found. Furthermore, Pt-pCVD-based samples revealed low overpotentials (between 9 and 10 mV vs. RHE) at low current densities when compared to the Pt/C reference electrocatalyst (≈ 17 mV vs. RHE). Remarkably, at high current densities a large Pt mass activity of 22.2 ± 1.2 A mg^{-1}$_{Pt}$ at an overpotential of 50 mV of the electrocatalyst prepared by using 250 pCVD pulses and 250 °C was recorded, outperforming the commercial Pt/C electrocatalyst by 40% and demonstrating increased Pt utilization. After optimization of the Pt electrode loading of MPNC$_C$-Pt-pCVD-250-250-T (0.9 µg$_{Pt}$ cm^{-2}$_{geo}$), an ultrahigh Pt mass activity of 56 ± 2 A mg^{-1}$_{Pt}$ at -50 mV vs. RHE was found, which is among the highest Pt mass activity for Pt cluster and single-atom based electrocatalysts reported so far. In summary, in-depth material characterization of MPNC-Pt-pCVD with ultra-high HER Pt mass activity synthesized by this pCVD method contributes to the emerging field of vapor-based synthesis for high-performance powder (electro)catalytic materials.

4. Experimental Section

Synthesis of Mesoporous N-Doped Carbon Nanospheres: A slightly changed synthesis of MPNC nanospheres was carried out according to our previous report.[6,17,34,35] In brief, SiO$_2$ nanoparticles (Ludox TMA, Sigma-Aldrich, 23 nm, 34 wt% in H$_2$O, 28.9 g) were dispersed in a hydrochloric acid solution (2793 mL, 0.1 м HCl) of Aniline (VWR, Analar Normapur, ≥99.5%, 94.2 mmol l^{-1}). Subsequently, hydrochloric acid solution (120 ml, 1 м) of dissolved ammonium persulfate (APS, Sigma-Aldrich, ≥98.0%, 2.2 mol l^{-1}) was added dropwise to the reaction mixture under vigorous stirring for 24 h in an ice bath. The obtained dark green solution was concentrated and washed by centrifugation until the supernatant reached a neutral pH value. The resulting composite PANI/SiO$_2$ material was freeze-dried and subsequently carbonized in a tube furnace (Carbolite Gero GmbH & Co. KG) under a constant N$_2$ gas flow of 120 ml min^{-1}. The material was heat-treated at 1000 °C for 6 h using a heat ramp of 200 °C h^{-1}. In order to remove the SiO$_2$ nanoparticles the MPNC/SiO$_2$ material was treated with a 4 м ammonium hydrogen difluoride solution (NH$_4$HF$_2$, Carl Roth, crystalline product dissolved in Milli-Q water, the highest safety precaution was required while working with this solution) and subsequently washed to pH neutrality. For the final washing step, MPNC was dispersed in ethanol (abs., VWR), stirred for 24 h, and dried in air. Finally, the MPNC product was heat treated at 1000 °C for 2 h under N$_2$ atmosphere with a heating ramp of 300 °C h^{-1}.

Pulsed Pt CVD on MPNC Nanospheres: Pt deposition was performed in a Kurt J. Lesker ALD-150LE reactor using a stop-flow, or static, precursor dosing process, where pumping of the process chamber was ceased immediately prior to a 1 s MeCpPtMe$_3$ (99%, Strem Chemicals, Inc.) pulse. Pumping of the process chamber did not resume until 30 s later. To prevent condensation of MeCpPtMe$_3$ in the precursor manifold, N$_2$ carrier gas flowed through the manifold causing an increase in the process chamber pressure up to ≈9 torr over the entire 31 s step. After the 31 s precursor exposure step, pumping of the process chamber was resumed and a 10 s purge step was performed. The pulse and purge steps were alternated and 50–250 total pulse-purge cycles were performed. The deposition temperature ranged from 225–300 °C. MeCpPtMe$_3$ was administered via vapor draw pulsing from a 50 ml stainless steel cylinder that was heated to 73 °C. Since this process involved only MeCpPtMe$_3$, N$_2$ as a carrier gas, and no co-reactants, it was considered pCVD.

During the deposition, MPNC samples were contained within a custom-made receptacle consisting of an aluminum well 1 cm in diameter and 0.5 cm deep (Scheme 1B). The well was covered with a porous aluminum oxide membrane filter with 0.2 µm diameter pores and a thickness of 60 µm (Sterlitech Corporation) to prevent the escape of MPNC powder. The membrane filter was held in place atop the well by a washer affixed with screws. Each receptacle was filled with 25 mg. To investigate the effects of total MPNC mass loaded into the ALD reactor, some depositions used multiple receptacles to reach a total mass of 50 mg of MPNC powder. Deposition denoted as MPNC$_A$ and MPNC$_C$ in the sample description used 25 mg and 50 mg of MPNC powder, respectively. To investigate the effects of the depth of the fixed powder bed on loading, dispersion, and morphology of Pt entities, the MPNC was separated into top and bottom fractions after each deposition. The top half, by mass, of the MPNC powder was removed and referred to as top (T) and the remaining bottom half was collected and referred to as bottom (B). For the clarity of sample description, the following sample code was used: MPNC$_{A/C}$-Pt-pCVD-*X*-*Y*-T/B, where *X* was the number of applied Pt-pCVD pulses, *Y* was the temperature of the reaction chamber in °C, A or C was the amount of MPNC used in mg (A: 25 mg MPNC; C: 50 mg MPNC) and T/B the sample position in the fixed bed, respectively.

Physical and Chemical Characterization: Scanning electron microscopy (SEM), transmission electron microscopy (TEM), and scanning transmission electron microscopy were performed. A field emission FEG-HRSEM SU8220 SEM (Hitachi) equipped with a transmission electron detector was used for imaging of MPNC nanospheres. High-resolution TEM and STEM images were taken on an FEI Talos F200X G2 (Thermo Fisher) operated at 200 kV. STEM tomography was performed using the same 200 kV FEI Talos F200X G2 equipped with a Fischione 2020 tomography holder. Tomograms were acquired using automatic routines (FEI STEM tomography software) with a linear tilt scheme in 1° steps and a range from −60° tilt to 60° tilt. A fast EDS mapping (1-minute acquisition time per image) was acquired for each tilt image. Reconstruction was performed using FEI inspect 4.5.1 software including the EDS tomograms. Image format conversion, stack de-interleaving, and brightness/contrast adjustments were performed using Image J 1.53c. For segmentation, ilastik 1.3.2 was used. Visualization was performed using Avizo for EM Systems 9.5.0. The aberration-corrected HAADF-STEM measurements were performed on a JEOL ARM300CF at the electron Physical Sciences Imaging Centre (ePSIC) located on the Harwell Campus in Oxfordshire in the Diamond Light Source facility. Unless otherwise stated microscopy measurements of MPNC and MPNC-Pt-pCVD were undertaken by wiping a copper 300 mesh holey carbon (Plano GmbH) or lacey carbon (Electron Microscopy Sciences) coated copper TEM grid through the respective sample powders.

The porous structure of MPNC was analyzed by nitrogen physisorption using a micro 300 (3P). Prior to measurement, MPNC was degassed at 100 °C under vacuum for two days. Isotherms were recorded at 77 K and surface area was calculated by applying the BET equation. Pore size distribution was obtained by fitting the adsorption branch of the isotherm with a quenched solid density function theory kernel (QuadraWin, Quantachrome) considering spherical, cylindrical, and slit pores of carbon material.

A Senterra II Raman microscope (Bruker Optics GmbH) equipped with a 532 nm laser (0.25 mW) was used for the recording of Raman spectra. The spectrum was a result of 500 cumulative scans with a wavenumber resolution of 4 cm^{-1}.

Quantitative bulk elemental composition of carbon, hydrogen, nitrogen, and sulfur was analyzed by thermal combustion of samples under O_2 at 1150 °C using a Vario MICRO Cube System (Elementar Analysensysteme GmbH) equipped with a thermal conductivity detector.

XPS spectra were collected using a SPECS EnviroESCA with a 1D delay line detector (1D-DLD) as an electron analyzer. A monochromatic Al Kα X-ray source ($h\nu = 1486.6$ eV) was used for the XPS measurements. A measurement was conducted with an X-ray source-to-analyzer angle of 55°. The sample was placed horizontally on the sample platform resulting in an electron-emission angle of 0°. XPS fitting was performed by using the XPSpeak41 software. The peak fitting of C1s, N1s, and O1s signal was based on a combined theoretical and experimental approach on N-doped chars reported previously.[67]

XRD patterns were collected on a Bruker D8 Discover (Bruker Corporation) with Cu-Kα radiation ($\lambda = 0.154187$ nm), variable divergence slit, and Lynxeye XE-T detector. The X-ray tube was operated at 40 kV and 40 mA. Samples were prepared on low background PMMA-silicon holders (Bruker) and measured in Bragg-Brentano geometry. The diffraction patterns were recorded from 10° to 105° (2Θ) using a step width of 0.025° and a step time of 0.5s.

TGA was conducted on a STA449 F5 (Netzsch Gerätebau GmbH) using a pre-heat-treatment step to 200 °C under N_2 atmosphere and a combustion step under air with a heating ramp of 2 °C min^{-1} and a temperature set point of 550 °C.

XAS data were collected in fluorescence modes at the KMC-3 beamline at the Helmholtz-Zentrum Berlin für Materialien und Energie BESSY II. The Pt L_3-edge spectra of Pt-pCVD-based samples and the corresponding references were recorded. The measured k^3-weighted EXAFS spectra $k^3\chi(k)$ were extracted by standard data reduction, absorption edge energy calibration, and background subtraction as implemented in ATHENA.[68] The spectra were reduced into the range $\Delta k \approx 3$-10 Å^{-1}, and Fourier transformed to FT$|k^3\chi(k)|$ into the real-space interval $\Delta R \approx 0$-6 Å. To calculate main values for interatomic distances, coordination numbers, and Debye-Waller factors (σ^2), nonlinear least-squares fitting of the FT$|k^3\chi(k)|$ spectra was carried out using ARTEMIS,[69] employing models for a Pt single atom, Pt metallic crystallographic structure, or PtO_2 crystallographic structure. These models were generated by ATOMS as implemented in IFEFFIT.[69] The amplitudes and phase shifts for single and multiple scattering paths were calculated using FEFF6.[69]

Electrochemical Characterization: A Biologic SP200 potentiostat was used for the electrochemical characterization and all measured potentials were compensated for ohmic losses by 85% based on the electrolyte resistance determined by electrochemical impedance spectroscopy (EIS) measurements at a high frequency of 100 kHz. The HER electrochemical activity tests, CO stripping experiments, and stability evaluations were performed in a temperature-controlled three-electrode cell. Thereby, the temperature was kept constant at 25 °C throughout the entire experiment. The working electrode was either an electrocatalyst-coated glassy carbon (GC) RDE (0.196 cm^2) for HER performance and CO stripping tests or a flat GC plate (0.76 cm^2) for HER stability evaluation, whereas a RHE from Gaskatel (Germany) and a Pt mesh (12 cm^2) were used as reference and counter electrodes, respectively.

For the deposition of a thin-film catalyst layer on the electrodes a catalyst ink was prepared by dispersing respectively 4.0, 2.3 and 3.6 mg of MPNC$_C$-Pt-pCVD-250-225-T, MPNC$_C$-Pt-pCVD-250-250-T and MPNC$_C$-Pt-pCVD-250-300-T in 1.2 ml of Milli-Q water (18.2 MΩ), 0.3 mL of high-purity isopropanol (99.9%, Sigma Aldrich) and 14.8, 7.8 and 12.8 µl of Nafion solution (5 wt%, Sigma Aldrich), respectively. 3.00 mg of the commercial reference electrocatalyst (Pt/C 20 wt%, HiSPEC3000, AlfaAesar) was added to 1.99 ml of Milli-Q water, 0.5 m of isopropanol and 10 µl of Nafion solution. The resulting ink dispersions with a constant ionomer-to-mass ratio of 0.18 were then homogenized with a horn sonifier (Branson 150) for 10 min. The catalyst inks were drop-cast on the RDE and subsequently dried at 400 rpm under ambient conditions and in an oven (Memmert GmbH) at 60 °C for 10 min, resulting in a Pt loading of 12.6 ± 0.2 µg$_{Pt}$ cm$^{-2}{}_{geo}$. Prior to activity measurements, the Pt-based thin-films were conditioned by cyclic voltammetry (CV). 50 voltammograms were recorded between 0.05 to 1 V versus RHE at 100 mV s^{-1} in 0.5 M H_2SO_4 electrolyte saturated with ultra-high purity N_2 (≥99.999%) and followed by 4 CV traces at 20 mV s^{-1} in the same potential range to compare hydrogen underpotential deposition features for ECSA determination. Cathodic polarization curves for the examination of the HER performance were collected at a rotation speed of 1600 rpm and a scanning speed of 5 mV s^{-1} in a 0.5 M H_2SO_4 electrolyte, which was saturated with ultra-high purity H_2 (≥99.999%, Sauerstoffwerk Friedrichshafen GmbH). Potentiostatic EIS measurements on the electrocatalysts were performed in H_2 saturated 0.5 M H_2SO_4 electrolyte and rotation of 1600 rpm at −10 mV versus RHE. A frequency range of 0.1 Hz to 100 kHz was used.

CO stripping experiments were performed in a 0.1 M $HClO_4$ electrolyte as the perchlorate was a non-adsorbing anion in contrast to the strongly adsorbing sulfate anion.[58] Prior to measurement, the catalyst electrode was conditioned between 0.05 and 1 V vs. RHE with 100 mV s^{-1} and 20 mV s^{-1} for 50 cycles and four cycles, respectively, in N_2 saturated electrolyte. Then, the electrolyte was saturated with CO (safety precautions were required when working with CO gas), and the catalyst-coated electrode was immersed in the electrolyte and rotated at 300 rpm. A chronoamperometry (CA) measurement was conducted by keeping a potential of 0.1 V versus RHE for 12 min. In the first 2 min CO was gently flushed through the electrolyte. N_2 purging was conducted for the remaining 10 min of the CA. The subsequent CV was performed in the N_2 saturated electrolyte without rotation between 0.05 and 1.2 V versus RHE with a scan rate of 20 mV s^{-1} and an initial potential of 0.1 V vs. RHE.

For HER stability measurements a flat glassy carbon electrode with a surface area of 0.76 cm^2 was used as H_2 gas bubble removal on an RDE under rotation for a long time might involve mechanical stress to the catalyst layer. The catalyst ink of $MPNC_C$-Pt-pCVD-250-250-T was drop-casted on the electrode so that the Pt loading was 12.6 µg $cm^2{}_{geo}$. Then the ink was dried under ambient conditions for 2 h and placed in an oven at 60 °C for 10 min. The resulting catalyst film was immersed in N_2-saturated 0.5 м H_2SO_4 and conditioned between 0.05 and 1 V vs. RHE with 100 mV s^{-1} for 50 cycles. The overpotential was recorded in the H_2 saturated electrolyte at two constant current densities (−10 mA $cm^{-2}{}_{geo}$ and −20 mA $cm^{-2}{}_{geo}$) for 8 h, respectively, by using chronopotentiometry.

Supporting Information

Supporting Information is available from the Wiley Online Library or from the author.

Acknowledgements

This work was financially supported by the Eva Mayr-Stihl Foundation within the Saltus!-program of the University of Freiburg (Saltus!-Group “Design of interfaces and interphases in energy materials”, University of Freiburg, grantee A.F.), the German Federal Ministry of Education and Research (BMBF, FKZ: 03SF0614A (CORAL-HD), grantee A.F.), the Volkswagen Foundation (Momentum – Funding for Recently Tenured Professors, “In-Situ Electrochemical Transmission Electron Microscopy – Understanding Electrocatalysts Dynamics under Electrochemical Conditions at the Nano Scale”, grantee A.F.), by the Deutsche Forschungsgemeinschaft (DFG, German Research Foundation) under Germany’s Excellence Strategy - EXC-2193/1 - 390951807 (grantee A.F), the U.S. National Science Foundation through The Pennsylvania State University 2D Crystal Consortium—Materials Innovation Platform (2DCC-MIP) under the NSF cooperative agreements DMR-1539916 and DMR-2039351 (I.E.C. and S.E.M.), The Pennsylvania State University Materials Research Science and Engineering Center (MRSEC) under the NSF cooperative agreement DMR-1420620 (I.E.C. and S.E.M.), a seed grant from The Pennsylvania State University (grantee S.E.M.), and the FRESCO program from DFG 422010107 ref. no. UP 14/1 (S.E.M.). Z.Z. appreciates further the state-funded scholarships of the Landesgraduiertenförderung of Baden Württemberg. Many thanks to Dr. Yi Thomann and Dr. Ralf Thomann from the Core Facility “Imaging of Materials Systems” at FIT for access to and training in electron microscopes. The authors acknowledge the BESSY II light source at the Helmholtz-Zentrum Berlin for providing beamtime at the KMC-3 beamline (proposal 20222077) and Dr. Michael Haumann for help at the beamline. The authors thank Diamond Light Source for access and support in the use of the electron Physical Science Imaging Centre (Instrument E02, proposal number MG33430) that contributed to the results presented here

Open access funding enabled and organized by Projekt DEAL.

Conflict of Interest

The authors declare no conflict of interest.

Data Availability Statement

The data that support the findings of this study are available from the corresponding author upon reasonable request.

Keywords

CO stripping, high Pt loading, hydrogen evolution reaction, Mesoporous N-doped carbon nanospheres, Pt clusters and single atoms, pulsed chemical vapor deposition, ultrahigh mass activity

Received: December 4, 2023
Revised: March 11, 2024

---

[1] M. Chatenet, B. G. Pollet, D. R. Dekel, F. Dionigi, J. Deseure, P. Millet, R. D. Braatz, M. Z. Bazant, M. Eikerling, I. Staffell, P. Balcombe, Y. Shao-Horn, H. Schäfer, *Chem. Soc. Rev.* **2022**, *51*, 4583.
[2] L. Deng, W. Hu, H. Deng, S. Xiao, *J. Phys. Chem. C* **2010**, *114*, 11026.
[3] N. G., E. Casals, I. Ojea, M. Varon, V. Puntes, in *The Delivery of Nanoparticles*, InTech, UK **2012**.
[4] W. J. Lee, S. Bera, C. M. Kim, E. K. Koh, W. P. Hong, S. J. Oh, E. A. Cho, S. H. Kwon, *NPG Asia Mater* **2020**, *12*, 40.
[5] M. Inaba, A. Zana, J. Quinson, F. Bizzotto, C. Dosche, A. Dworzak, M. Oezaslan, S. B. Simonsen, L. T. Kuhn, M. Arenz, *ACS Catal.* **2021**, *11*, 7144.
[6] Z. Zeng, S. Küspert, S. E. Balaghi, H. E. M. Hussein, N. Ortlieb, M. Knäbbeler-Buß, P. Hügenell, S. Pollitt, N. Hug, J. Melke, A. Fischer, *Small* **2023**, *19*, 2205885.
[7] K. Zhang, X. Liang, L. Wang, K. Sun, Y. Wang, Z. Xie, Q. Wu, X. Bai, M. S. Hamdy, H. Chen, X. Zou, *Nano Res. Energy* **2022**, *1*, 9120032.
[8] Y. Yu, R. Liu, Y. Sun, Z. Liu, X. Shi, J. Lai, L. Wang, *Mater. Chem. Front.* **2023**, *8*, 159.
[9] L. Zhang, Q. Wang, R. Si, Z. Song, X. Lin, M. N. Banis, K. Adair, J. Li, K. Doyle-Davis, R. Li, L. M. Liu, M. Gu, X. Sun, *Small* **2021**, *17*, 2004453.
[10] Z. Song, Y. N. Zhu, H. Liu, M. N. Banis, L. Zhang, J. Li, K. Doyle-Davis, R. Li, T. K. Sham, L. Yang, A. Young, G. A. Botton, L. M. Liu, X. Sun, *Small* **2020**, *16*, 2003096.
[11] M. H. Suliman, A. Adam, M. N. Siddiqui, Z. H. Yamani, M. Qamar, *Catal. Sci. Technol.* **2019**, *9*, 1497.
[12] P. Yin, L.-J. Zuo, W.-J. Zeng, M. Zuo, L. Tong, X.-Z. Fu, H.-W. Liang, *Appl. Catal. B* **2023**, *328*, 122543.
[13] A. Gunnarson, J. De Bellis, T. Imhof, N. Pfänder, M. Ledendecker, F. Schüth, *Chem. Mater.* **2006**, *35*, 2023
[14] A. P. Amrute, J. De Bellis, M. Felderhoff, F. Schüth, *Chem. – Eur. J.* **2021**, *27*, 6819.
[15] P. Munnik, P. E. De Jongh, K. P. De Jong, *Chem. Rev.* **2015**, *115*, 6687.
[16] M. J. Ndolomingo, N. Bingwa, R. Meijboom, *J. Mater. Sci.* **2020**, *55*, 6195.
[17] J. Melke, R. Schuster, S. Möbus, T. Jurzinsky, P. Elsässer, A. Heilemann, A. Fischer, *Carbon N Y* **2019**, *146*, 44.
[18] R. J. Ouimet, T. A. Ebaugh, G. Mirshekari, S. Bliznakov, L. J. Bonville, R. Maric, *Energy and Fuels* **2021**, *35*, 1933.
[19] N. Cheng, S. Stambula, D. Wang, M. N. Banis, J. Liu, A. Riese, B. Xiao, R. Li, T. K. Sham, L. M. Liu, G. A. Botton, X. Sun, *Nat. Commun.* **2016**, *7*, 13638.
[20] F. Grillo, H. Van Bui, J. A. Moulijn, M. T. Kreutzer, J. R. Van Ommen, *J. Phys. Chem. Lett.* **2017**, *8*, 975.
[21] D. S. Choi, A. W. Robertson, J. H. Warner, S. O. Kim, H. Kim, *Adv. Mater.* **2016**, *28*, 7115.
[22] J. Li, X. Liang, D. M. King, Y. B. Jiang, A. W. Weimer, *Appl. Catal. B* **2010**, *97*, 220.
[23] J. Hämäläinen, M. Ritala, M. Leskelä, *Chem. Mater.* **2014**, *26*, 786.
[24] W. Setthapun, W. D. Williams, S. M. Kim, H. Feng, J. W. Elam, F. A. Rabuffetti, K. R. Poeppelmeier, P. C. Stair, E. A. Stach, F. H. Ribeiro, J. T. Miller, C. L. Marshall, *J. Phys. Chem. C* **2010**, *114*, 9758.
[25] R. R. Hoover, Y. V. Tolmachev, *J. Electrochem. Soc.* **2009**, *156*, A37.
[26] S. Stambula, N. Gauquelin, M. Bugnet, S. Gorantla, S. Turner, S. Sun, J. Liu, G. Zhang, X. Sun, G. A. Botton, *J. Phys. Chem. C* **2014**, *118*, 3890.
[27] T. Aaltonen, M. Ritala, T. Sajavaara, J. Keinonen, M. Leskelä, *Chem. Mater.* **1924**, *15*, 2003.

[28] J. S. King, A. Wittstock, J. Biener, S. O. Kucheyev, Y. M. Wang, T. F. Baumann, S. K. Giri, A. V. Hamza, M. Baeumer, S. F. Bent, *Nano Lett.* **2008**, *8*, 2405.

[29] J. Dendooven, R. K. Ramachandran, K. Devloo-Casier, G. Rampelberg, M. Filez, H. Poelman, G. B. Marin, E. Fonda, C. Detavernier, *J. Phys. Chem. C* **2013**, *117*, 20557.

[30] H. Kim, S. H. Moon, *Carbon N Y* **2011**, *49*, 1491.

[31] Z. Cai, B. Liu, X. Zou, H. M. Cheng, *Chem. Rev.* **2018**, *118*, 6091.

[32] H. Y. Kim, S. J. Lee, N. J. Jung, *Solid State Phenomena* **2007**, *124–126*, 1769.

[33] A. M. Lubers, C. L. Muhich, K. M. Anderson, A. W. Weimer, *J. Nanoparticle Res.* **2015**, *17*, 179.

[34] T. Berestok, C. Diestel, N. Ortlieb, S. W. Glunz, A. Fischer, *Adv. Mater. Technol.* **2022**, *7*, 2200237.

[35] J. Melke, J. Martin, M. Bruns, P. Hu, A. Scho, A. Fischer, S. M. Isaza, F. Fink, P. Elsa, *ACS Appl. Energy Mater* **2020**, *3*, 11627.

[36] K. Momma, F. Izumi, *J. Appl. Crystallogr.* **2011**, *44*, 1272.

[37] S. Popović, *Crystals* **2020**, *10*, 27.

[38] Z. Xue, H. Thridandam, H. D. Kaesz, R. F. Hicks, *Chem. Mater.* **1992**, *4*, 162.

[39] A. J. M. MacKus, N. Leick, L. Baker, W. M. M. Kessels, *Chem. Mater.* **2012**, *24*, 1752.

[40] I. E. Campbell, N. Nayir, A. C. T. Van Duin, S. E. Mohney, *J. Phys. Chem. C* **2022**, *126*, 16357.

[41] J. Ji, Y. Zhang, L. Tang, C. Liu, X. Gao, M. Sun, J. Zheng, M. Ling, C. Liang, Z. Lin, *Nano Energy* **2019**, *63*, 103849.

[42] P. Kuang, Y. Wang, B. Zhu, F. Xia, C. Tung, J. Wu, H. M. Chen, J. Yu, *Adv. Mater.* **2021**, *33*, 2008599.

[43] H. Zhang, P. An, W. Zhou, B. Y. Guan, P. Zhang, J. Dong, X. W. (David) Lou, *Sci. Adv.* **2018**, *4*, aao6657.

[44] T. Li, J. Liu, Y. Song, F. Wang, *ACS Catal.* **2018**, *8*, 8450.

[45] G. Zhang, D. Yang, E. Sacher, *J. Phys. Chem. C* **2007**, *111*, 565.

[46] M. Y. Smirnov, A. V. Kalinkin, E. I. Vovk, P. A. Simonov, E. Y. Gerasimov, A. M. Sorokin, V. I. Bukhtiyarov, *Appl. Surf. Sci.* **2018**, *428*, 972.

[47] J. Ma, A. Habrioux, Y. Luo, G. Ramos-Sanchez, L. Calvillo, G. Granozzi, P. B. Balbuena, N. Alonso-Vante, *J Mater Chem A Mater* **2015**, *3*, 11891.

[48] S. Yang, J. Kim, Y. J. Tak, A. Soon, H. Lee, *Angew. Chem.* **2016**, *128*, 2098.

[49] B. Qiao, A. Wang, X. Yang, L. F. Allard, Z. Jiang, Y. Cui, J. Liu, J. Li, T. Zhang, *Nat. Chem.* **2011**, *3*, 634.

[50] A. N. Mansour, D. E. Sayers, J. W. Cook, D. R. Short, R. D. Shannon, J. R. Katzer, X-Ray Absorption Studies of Some Platinum Oxides, **1984**.

[51] M. Brown, R. E. Peierls, E. A. Stern, *Phys. Rev. B* **1977**, *15*, 738.

[52] S. S. Hardisty, X. Lin, A. R. J. Kucernak, D. Zitoun, *Carbon Energy* **2023**, *6*, 409.

[53] C. Wang, H. Zang, C. Liu, J. Wang, L. Kuai, B. Geng, *Inorg. Chem.* **2023**, *62*, 6856.

[54] J. J. L. Mulders, L. M. Belova, A. Riazanova, *Nanotechnology* **2011**, *22*, 055302.

[55] A. M. Funtikov, U. Stimming, R. Vogel, *J. Electroanal. Chem.* **1997**, *428*, 147.

[56] F. C. Nart, T. Iwasita, M. Weber, *Electrochim. Acta* **1994**, *39*, 2093.

[57] J. Clavilier, D. Armand, S. G. Sun, M. Petit, *J. Electroanal. Chem. Interfacial Electrochem.* **1986**, *205*, 267.

[58] G. A. Kamat, J. A. Zamora Zeledón, G. T. K. K. Gunasooriya, S. M. Dull, J. T. Perryman, J. K. Nørskov, M. B. Stevens, T. F. Jaramillo, *Commun Chem* **2022**, *5*, 20.

[59] E. G. Ciapina, S. F. Santos, E. R. Gonzalez, *J. Electroanal. Chem.* **2018**, *815*, 47.

[60] M. Arenz, K. J. J. Mayrhofer, V. Stamenkovic, B. B. Blizanac, T. Tomoyuki, P. N. Ross, N. M. Markovic, *J. Am. Chem. Soc.* **2005**, *127*, 6819.

[61] F. Maillard, M. Eikerling, O. V. Cherstiouk, S. Schreier, E. Savinova, U. Stimming, *Faraday Discuss.* **2004**, *125*, 357.

[62] W. F. Chen, C. H. Wang, K. Sasaki, N. Marinkovic, W. Xu, J. T. Muckerman, Y. Zhu, R. R. Adzic, *Energy Environ. Sci.* **2013**, *6*, 943.

[63] G. F. Wei, Z. P. Liu, *Chem. Sci.* **2015**, *6*, 1485.

[64] A. Lasia, *Int. J. Hydrogen Energy* **2019**, *44*, 19484.

[65] J. N. Hansen, H. Prats, K. K. Toudahl, N. Mørch Secher, K. Chan, J. Kibsgaard, I. Chorkendorff, *ACS Energy Lett.* **2021**, *6*, 1175.

[66] X. Cheng, B. Xiao, Y. Chen, Y. Wang, L. Zheng, Y. Lu, H. Li, G. Chen, *ACS Catal.* **2022**, *12*, 5970.

[67] M. Ayiania, M. Smith, A. J. R. Hensley, L. Scudiero, J. S. McEwen, M. Garcia-Perez, *Carbon N Y* **2020**, *162*, 528.

[68] B. Ravel, M. Newville, *J. Synchrotron Radiat.* **2005**, *12*, 537.

[69] A. L. Ankudinov, B. Ravel, J. J. Rehr, S. D. Conradson, *Phys. Rev. B* **1998**, *58*, 7565.